Please cite this article in press as: Vandervore et al., TMX2 Is a Crucial Regulator of Cellular Redox State, and Its Dysfunction Causes Severe Brain Developmental Abnormalities, The American Journal of Human Genetics (2019), https://doi.org/10.1016/j.ajhg.2019.10.009

ARTICLE

TMX2 Is a Crucial Regulator of Cellular Redox State, and Its Dysfunction Causes Severe Brain Developmental Abnormalities

Laura V. Vandervore,[1,2,3,42] Rachel Schot,[1,42] Chiara Milanese,[4] Daphne J. Smits,[1] Esmee Kasteleijn,[1] Andrew E. Fry,[5,6] Daniela T. Pilz,[7] Stefanie Brock,[2,8] Esra Börklü-Yücel,[1,9,10] Marco Post,[9] Nadia Bahi-Buisson,[11] María José Sánchez-Soler,[12] Marjon van Slegtenhorst,[1] Boris Keren,[13] Alexandra Afenjar,[14] Stephanie A. Coury,[15] Wen-Hann Tan,[15,16] Renske Oegema,[17] Linda S. de Vries,[18] Katherine A. Fawcett,[19,41] Peter G.J. Nikkels,[20] Aida Bertoli-Avella,[21] Amal Al Hashem,[22] Abdulmalik A. Alwabel,[23] Kalthoum Tlili-Graiess,[24] Stephanie Efthymiou,[25] Faisal Zafar,[26] Nuzhat Rana,[26] Farah Bibi,[27] Henry Houlden,[25] Reza Maroofian,[25] Richard E. Person,[28] Amy Crunk,[28]

(Author list continued on next page)

The redox state of the neural progenitors regulates physiological processes such as neuronal differentiation and dendritic and axonal growth. The relevance of endoplasmic reticulum (ER)-associated oxidoreductases in these processes is largely unexplored. We describe a severe neurological disorder caused by bi-allelic loss-of-function variants in thioredoxin (TRX)-related transmembrane-2 (*TMX2*); these variants were detected by exome sequencing in 14 affected individuals from ten unrelated families presenting with congenital microcephaly, cortical polymicrogyria, and other migration disorders. *TMX2* encodes one of the five TMX proteins of the protein disulfide isomerase family, hitherto not linked to human developmental brain disease. Our mechanistic studies on protein function show that TMX2 localizes to the ER mitochondria-associated membranes (MAMs), is involved in posttranslational modification and protein folding, and undergoes physical interaction with the MAM-associated and ER folding chaperone calnexin and ER calcium pump SERCA2. These interactions are functionally relevant because *TMX2*-deficient fibroblasts show decreased mitochondrial respiratory reserve capacity and compensatory increased glycolytic activity. Intriguingly, under basal conditions TMX2 occurs in both reduced and oxidized monomeric form, while it forms a stable dimer under treatment with hydrogen peroxide, recently recognized as a signaling molecule in neural morphogenesis and axonal pathfinding. Exogenous expression of the pathogenic *TMX2* variants or of variants with an *in vitro* mutagenized TRX domain induces a constitutive TMX2 polymerization, mimicking an increased oxidative state. Altogether these data uncover TMX2 as a sensor in the MAM-regulated redox signaling pathway and identify it as a key adaptive regulator of neuronal proliferation, migration, and organization in the developing brain.

Introduction

The endoplasmic reticulum (ER) is responsible for the folding of one third of the human proteome. Protein folding is coordinated by ER chaperones, together with ER oxidoreductases of the protein disulfide isomerase (PDI) family.[1] This family consists of 23 oxidoreductase proteins[2] and is part of the thioredoxin (TRX) superfamily.[3] PDIs are characterized by the presence of at least one TRX-like domain (potentially catalytically active with a

[1]Department of Clinical Genetics, Erasmus University Medical Center, PO Box 2040, 3000 CA Rotterdam, the Netherlands; [2]Neurogenetics Research Group, Research Cluster Reproduction, Genetics and Regenerative Medicine, Vrije Universiteit Brussel, Brussels 1090, Belgium; [3]Center for Medical Genetics, UZ Brussel, Brussels 1090, Belgium; [4]Department of Molecular Genetics, Erasmus University Medical Center, PO Box 2040, 3000 CA Rotterdam, the Netherlands; [5]Institute of Medical Genetics, University Hospital of Wales, Cardiff CF14 4XW, UK; [6]Division of Cancer and Genetics, School of Medicine, Cardiff University, Cardiff CF14 4XN, UK; [7]West of Scotland Clinical Genetics Service, Queen Elizabeth University Hospital, Glasgow G51 4TF, UK; [8]Department of Pathology, UZ Brussels, Brussels 1090, Belgium; [9]Department of Cell Biology, Erasmus University Medical Center, PO Box 2040, 3000 CA Rotterdam, the Netherlands; [10]Medical Genetics Department, Koç University School of Medicine, Istanbul 34010, Turkey; [11]Imagine Institute, INSERM UMR-1163, Laboratory Genetics and Embryology of Congenital Malformations, Paris Descartes University, Institut des Maladies Génétiques 24, Boulevard de Montparnasse, Paris 75015, France; [12]Sección Genética Médica, Servicio de Pediatría, Hospital Clínico Universitario Virgen de la Arrixaca, IMIB-Arrixaca, Murcia 30120, España; [13]Département de génétique, Hôpital Pitié-Salpêtrière, Assistance Publique – Hôpitaux de Paris, Paris 75013, France; [14]Département de génétique et embryologie médicale, CRMR des malformations et maladies congénitales du cervelet et des déficits intellectuels de causes rares, GRC n°19, pathologies Congénitales du Cervelet-LeucoDystrophies, Sorbonne Universités, Hôpital Trousseau, Paris 75012, France; [15]Division of Genetics and Genomics, Boston Children's Hospital, Boston, MA 02115, USA; [16]Harvard Medical School, Boston, MA 02115, USA; [17]Department of Genetics, University Medical Center Utrecht, Utrecht University, 3584 CX, the Netherlands; [18]Department of Neonatology, University Medical Center Utrecht, Utrecht University, 3584 CX, the Netherlands; [19]Medical Research Council (MRC) Computational Genomics Analysis and Training Programme, MRC Centre for Computational Biology, MRC Weatherall Institute of Molecular Medicine, John Radcliffe Hospital, Headington, Oxford OX3 9DS, UK; [20]Department of Pathology, University Medical Center Utrecht, Utrecht University, 3584 CX, the Netherlands; [21]Centogene AG, Rostock 18055, Germany; [22]Division of Medical Genetic, Department of Pediatrics, Prince Sultan Military Medical City, Riyadh 12233, Saudi Arabia; [23]Division of General Pediatrics, Department of Pediatrics, Prince Sultan Military Medical City, Riyadh 12233, Saudi Arabia; [24]Division of Neuroradiology, Department of Radiology, Prince Sultan Military Medical City, Riyadh 12233, Saudi Arabia; [25]Department of Neuromuscular Disorders, University College London Institute of Neurology, Queen Square, London WC1N 3BG, UK; [26]Department of Pediatric Neurology, Children's Hospital and Institute of Child Health, Multan 60000, Pakistan; [27]University Institute of Biochemistry & Biotechnology, PMAS – Arid Agriculture University,

(Affiliations continued on next page)

Please cite this article in press as: Vandervore et al., TMX2 Is a Crucial Regulator of Cellular Redox State, and Its Dysfunction Causes Severe Brain Developmental Abnormalities, The American Journal of Human Genetics (2019), https://doi.org/10.1016/j.ajhg.2019.10.009

Juliann M. Savatt,[29] Lisbeth Turner,[29] Mohammad Doosti,[30] Ehsan Ghayoor Karimiani,[31,32] Nebal Waill Saadi,[33] Javad Akhondian,[34] Maarten H. Lequin,[35] Hülya Kayserili,[10] Peter J. van der Spek,[36] Anna C. Jansen,[2,37] Johan M. Kros,[38] Robert M. Verdijk,[38] Nataša Jovanov Milošević,[39] Maarten Fornerod,[9] Pier Giorgio Mastroberardino,[4,40] and Grazia M.S. Mancini[1,*]

sequence including two cysteines, C-X-X-C) and an ER retention domain (typically Lys-Asp-Glu-Leu/KDEL).[3,4] In the oxidizing environment of the ER, PDIs with active site cysteines can oxidize thiol groups of newly synthesized polypeptides mediating protein folding,[2,5] but they can also catalyze reduction and isomerization of disulfides in misfolded proteins, facilitating ER-associated degradation (ERAD) during the unfolded protein response (UPR).[6]

PDI-mediated protein folding is ATP dependent and relies on precise regulation of calcium influx to the mitochondria, necessary for mitochondrial oxidative phosphorylation.[1,7] Because the ER is the major storage site for calcium, specialized ion channels, e.g., sarcoplasmic-endoplasmic reticulum Ca^{2+}-ATPase ATP2A2/SERCA2, inositol 1,4,5 trisphosphate receptor type 1 (IP3R1), and voltage-dependent anion-selective channel 1 (VDAC1), are located at the mitochondria-associated membranes (MAMs) of the ER to assure proper calcium transport to and from the ER.[1] Besides regulating protein folding, some PDI oxidoreductases additionally function in calcium trafficking through interaction with these ER calcium channels.[1,8,9] Accordingly, some PDIs show enriched ER localization at the MAM.[10] Through upregulation of calcium transport into the mitochondria, PDIs are also able to regulate ATP production, which is necessary to increase folding mechanisms when misfolded proteins aggregate (ER-stress).[1,7,11] Hence, PDIs and protein folding are important determinants for normal mitochondrial bioenergetics and cell survival.

In humans, altered expression of PDIs has been correlated with neurodegenerative disorders like Alzheimer disease, Parkinson disease, and amyotrophic lateral sclerosis.[12] However, notwithstanding their proven biological relevance, little is known about the consequence of inherited pathogenic variants in PDIs. At the moment of writing, only one heterozygous recurrent *P4HB* variant (OMIM: 176790) (Prolyl 4-hydroxylase, β-subunit) encoding PDIA1 has been associated with Cole-Carpenter syndrome 1 (OMIM: 112240), characterized by skeletal malformations (OMIM: 176790).[12–15] Pathogenic variants in non-PDI oxidoreductases from other protein families, e.g., *WWOX* (OMIM: 605131),[16] *DHCR24* (OMIM: 606418),[17] and *NDUFS1* (OMIM: 157655),[18] and variants in MAM-associated genes, e.g., *SERAC1* (OMIM: 614725)[19] and *MFN2* (OMIM: 608507),[20] have been linked to neurodevelopmental and mitochondrial disorders.

Thioredoxin (TRX)-related transmembrane proteins (TMX) are five type 1 transmembrane proteins belonging to the PDI family.[2,3,21] The best studied of the group, TMX1 (PDIA11), is localized at the MAM and regulates calcium trafficking through interaction with the ER calcium pump SERCA2.[1,7] No pathogenic variants have been reported in TMX members in relation to human disease until now, although two missense variants of unknown significance in *TMX3* were proposed to lead to microphthalmia.[22] TMX2 (PDIA12), one of the least studied of the group, is encoded by *TMX2* on chromosome 11q12.1 (OMIM: 616715), is ubiquitously expressed, and presents in two isoforms; the longest, with 296 amino acids, is the most biologically relevant as an ER resident protein.[21] The N-terminal signal sequence (amino acid 1–48) is followed by the cytosolic domain (amino acid 49–102), the single transmembrane domain (amino acid 103–125), the atypical TRX domain (amino acid 167–170, Ser-Asn-Asp-Cys, SNDC), the ER intraluminal C-terminal domain (amino acid 126–296), and a Di-lysine ER retention motif (amino acid 293–296, Lys-Lys-Asp-Lys, KKDK).[3,4] It has been suggested that TMX2 is enriched at the MAM location.[10] Because TMX2 does not contain a typical thioredoxin-like active domain (SNDC instead of CXXC), its oxidoreductase activity and role in protein folding have been questioned. However, the importance of *TMX2* is underlined by the non-viability of homozygous *Tmx2*−/− knockout mice (C57BL/6NJ strain, Mouse Genome Informatics MGI: 1914208). Here we report microcephaly, polymicrogyria (PMG), complex migration disorders, and epilepsy in individuals bearing bi-allelic, autosomal-recessive variants in *TMX2*. We study the function of normal TMX2 and the effect of the variants in human cells, providing a mechanistic

Rawalpindi 43600, Pakistan; [28]GeneDx, 207 Perry Parkway, Gaithersburg, MD 20877, USA; [29]The Autism & Developmental Medicine Institute at Geisinger, Danville, PA 17822, USA; [30]Department of Molecular Genetics, Next Generation Genetic Polyclinic, Mashhad 009851, Iran; [31]Molecular and Clinical Sciences Institute, St. George's, University of London, Cranmer Terrace London, SW17 ORE, UK; [32]Innovative Medical Research Center, Mashhad Branch, Islamic Azdad University, Mashhad 9133736351, Iran; [33]College of Medicine / Baghdad University, Children Welfare Teaching Hospital, Medical City Complex, Baghdad 10001, Iraq; [34]Department of Pediatric Neurology, Ghaem Hospital, Mashhad University of Medical Sciences, Mashhad 009851, Iran; [35]Department of Radiology, University Medical Center Utrecht, Utrecht, 3584 CX, the Netherlands; [36]Department of Pathology, Clinical Bio-informatics, Erasmus University Medical Center, PO Box 2040, 3000 CA Rotterdam, the Netherlands; [37]Pediatric Neurology Unit, Department of Pediatrics, Universitair Ziekenhuis Brussel, Brussels 1090, Belgium; [38]Department of Pathology, Erasmus University Medical Center, PO Box 2040, 3000 CA Rotterdam, the Netherlands; [39]Croatian Institute of Brain Research, School of Medicine, University of Zagreb, Zagreb 10000, Croatia; [40]Department of Life, Health and Environmental Sciences, University of L'Aquila, L'Aquila 67100, Italy
[41]Present address: Department of Health Sciences, University of Leicester, George Davies Centre, University Road, Leicester LE1 7RH, UK
[42]These authors contributed equally to this work
*Correspondence: g.mancini@erasmusmc.nl
https://doi.org/10.1016/j.ajhg.2019.10.009.

Please cite this article in press as: Vandervore et al., TMX2 Is a Crucial Regulator of Cellular Redox State, and Its Dysfunction Causes Severe Brain Developmental Abnormalities, The American Journal of Human Genetics (2019), https://doi.org/10.1016/j.ajhg.2019.10.009

understanding of TMX2 function in health and disease and linking PDIs to neurodevelopment.

Material and Methods

Ethics Statement and Biopsy

The cohort of *TMX2*-variant affected individuals (here coded as P1 to P14) includes 10 families, of which four were gathered through the European Network on Brain Malformations, Neuro-MIG (COST Action CA16118), five families were gathered through GeneMatcher,[23] and one family was earlier described in supplemental data from a cohort of undiagnosed individuals with malformations of cortical development.[24] All study participants or their legal caretakers gave written informed consent to participate in this study and for publication of images, according to Erasmus MC institutional review board requirements (protocol METC-2012387). Skin biopsies were sampled before the study for routine diagnostic purposes and used to isolate dermal fibroblasts via standard procedures. Fibroblasts were tested negative for mycoplasma infection.

Neuropathology

Autopsies that included the brain were performed after the demises of individual P1 at 14 days of age and individual P10 at two days of age. The material was fixed in 4% formalin. Samples from the frontal, parietal, temporal, and occipital lobes, deep nuclei, the cerebellum, the brain stem, and the spinal cord were submitted for histological evaluation. Paraffin-embedded samples were cut to a thickness of 5 μm, and hematoxylin and eosin-staining (H&E) or Lugol-PAS (periodate-Schiff staining) were performed according to the manufacturer's guidelines (Hoffmann-LaRoche). For the age- and gender-matched control brain, the sample collection was approved by the institutional ethical review board (EP02/21AG) of the Clinical Hospital Centre and School of Medicine, the University of Zagreb, in accordance with the Helsinki declaration 2000, and the samples became a part of the Zagreb Neuroembryological Collection.[25]

Genomic and Transcriptomic Analysis

Whole-Exome Sequencing

DNA was isolated from blood of the probands and family members and used for exome and Sanger sequencing in nine different laboratories. Whole-exome sequencing (WES) data are deposited internally at the Erasmus MC and in each medical institute that referred the individuals with *TMX2* variants, in respect to the privacy of the families. Details of sequencing and analysis pipelines are described in the Supplemental Data.

RNA Sequencing

Skin fibroblasts from affected individuals P1 and P2 and four different healthy age- and sex- (male) matched controls were cultured to 80% confluence in T175 flasks, then subjected to RNA isolation with TRIzol Reagent (Invitrogen, 15596026) and RNA cleanup with the RNeasy mini kit (QIAGEN, 74106). The samples were processed with the NEBNext Ultra Directional RNA Library Prep Kit for Illumina. Strand-specific mRNA-seq libraries for the Illumina platform were generated with a poly-A selection and sequenced at GenomeScan. Fastq files from forward and reverse reads were aligned to reference genome hg38 with the STAR aligner tool (v.2.4.2a).[26] Counts per gene were calculated from bam files via the featureCount program with version 27 of the genecode hg38 annotation.[27] For differential gene expression, P1 and P2's samples were compared to four male control samples in R (v.3.4.3) (see Web Resources) using the edgeR package (v.3.20.9).[28] Functional annotation clustering of the top 1,000 differentially expressed genes ($p < 0.05$) was performed with the gene ontology Database for Annotation, Visualization and Integrated Discovery (DAVID, v6.8).[29,30] Downstream affected biological functions were determined with Ingenuity pathway analysis (IPA, QIAGEN, versus2018) on all differentially expressed genes with a p value below 0.05.

qPCR

Skin fibroblasts were cultured in T75 culture flasks in DMEM with 10% fetal calf serum (FCS), 1% PenStrep, Lonza (DMEM with serum), to 80% confluence. Total RNA was extracted on RNeasy mini columns (QIAGEN, 74106) according to the manufacturer's protocol. Reverse transcription was performed on 1 μg of RNA in a total volume of 20 μl with the iScript cDNA Synthesis kit (Bio-Rad Laboratories) used according to the manufacturer's instructions. Real-time quantitative polymerase chain reaction (RT-qPCR) was performed with iTaq Universal SYBR Green Supermix (Bio-Rad Laboratories) according to the manufacturer's instructions. Primers for RT-qPCR analysis for the experiments shown in Figure 3 are listed in Table S1.

Antibodies

Primary antibodies used: polyclonal Rabbit anti-human TMX2 (HPA040282, Sigma, WB 1:250), monoclonal rabbit anti-human HSP60 (D6F1, Cell Signaling Technologies, Immunocytochemistry [ICC] dilution 1:800), monoclonal rabbit anti-human CNX (C5C9, Cell Signaling Technologies, ICC 1:50, IP 1:1000), mouse monoclonal anti-SERCA2 ATPase (ab2861, Abcam IP:1:1000), mouse monoclonal anti-Myc (9B11, Cell Signaling Technologies, WB 1:3000 and ICC 1:500), and mouse monoclonal anti-PDI (1D3, ADI-SPA-891, Enzo Life Sciences, WB: 1:1000).

Secondary antibodies used for ICC: green goat anti-rabbit IgG (H+L) Alexa Fluor 488 (1:400, Thermo Fisher Scientific, A11088) and red Cy3 AffiniPure donkey anti-mouse IgG (H+L) (1:100, Jackson Laboratories, 715-165-150). Secondary antibodies used for WB in 1 in 10 000: red IRDye 680RD goat anti-rabbit IgG (H+L) (LI-COR Biosciences, 926-68071) and green IRDye 800CW goat anti-mouse IgG (H+L) (LI-COR Biosciences, 926-32210).

Plasmid Constructs

Wild-type human *TMX2* (GenBank: NM_015959.3) was cloned in a pCMV-Entry-Myc-DDK TrueORF Gold vector (OriGene, RC200032). 50 μL semi-competent homemade *Escherichia coli* XL10-Gold Bacteria strains were thawed on ice for 20 min and subsequently incubated for 15 min with 0.1 μg wild-type *TMX2* plasmid. Transformation of the bacterial cells was induced through a heat shock at 42°C for 2 min. 800 μL Luria-Bertani (LB) broth (EZ Mix, Lennox) was added to the cells and placed under agitation (200 rpm, 40 min, 37°C). The selection of transformed cells was performed overnight on LB-Kanamycin agar plates at 37°C. Vector-positive colonies were grown to 50 mL midiprep. Plasmid DNA was isolated with the QIAGEN Plasmid Plus Midi kit. The full length and sequence of *TMX2* cDNA in the plasmid was checked by capillary sequencing before the transfections were performed. pcDNA3.1/Myc-His (-)/LacZ (Thermo Fisher Scientific) was used as a negative control and kindly provided by Dr. Mark Nellist.

Site-Directed Mutagenesis

Variant *TMX2* constructs (TRX domain SNDC to SNDG p.Cys170Gly [c.508T>G] and affected individuals' variants p.Arg53Cys [c.157C>T] and p.Arg231Trp [c.691C>T]) were generated according to manufacturers' procedures via the QuikChange II XL Site-Directed Mutagenesis Kit (Agilent), wild-type purified *TMX2* construct dilution (10 ng/μL), and 100 ng/μL primers specified in Table S2. PCR products were transformed in ultracompetent

Escherichia coli XL10-Gold bacteria supplemented with β-mercaptoethanol in S.O.C. (super optimal broth) medium through a heat shock at 42°C for 30 s. Selection, midi isolation, and Sanger sequencing were performed in analogy with the wild-type construct.

Sanger Sequencing of Plasmid DNA

Sanger sequencing of wild-type and variant plasmid DNA was performed as earlier described.[31] In brief, amplification reactions were performed in a total volume of 20 μl, containing 1 × PCR buffer with Mg (Roche), 200 μM of each deoxyribonucleotide triphosphate (dNTP), 1 μM forward and reverse primer (specified in Table S3), 0.1 units of Fast Start Taq DNA polymerase (Roche), and 25 ng genomic DNA. PCR conditions were as follows: 5′ 96°C, 10 cycles of 30″ 96°C, 30″ 68°C (−1°C/cycle), 60″ 72°C, then 25 cycles of 30″ 96°C, 30″ 58°C, 60″ 72°C, and a final extension for 5′ 72°C.

PCR reactions were purified with ExoSAP-IT (USB). Direct sequencing of both strands was performed with Big Dye Terminator chemistry (version 3.1; Applied Biosystems). DNA fragment analysis was performed with capillary electrophoresis on an ABI 3130 Genetic Analyzer (Applied Biosystems) with the software package Seqscape (Applied Biosystems, version 2.1).

Transfection

Human embryonic kidney HEK293T cells were plated at 5 × 10^4 cells/cm^2 with or without 24 mm coverslips (Thermo Fisher Scientific) cultured in 2 mL DMEM with serum in a 6-well plate or 10 cm Petri dishes for immunoprecipitation (IP). The next day, culture medium was replaced with 2 mL DMEM without serum (Lonza). Per 10 cm^2, 1 μg plasmid DNA was added to 125 μL DMEM without serum at room temperature, and 3 μL/10cm^2 Lipofectamine 2000 Transfection Reagent (Thermo Fisher Scientific) was added to 125 μL DMEM without serum. These tubes mixed and incubated for 5 min at room temperature prior to transfection. The appropriate volume was added to each dish in a dropwise manner. After 3 h, 10% FCS and 1% PenStrep was supplemented to the dishes. After 24 h transfection, cells were fixated with methanol for 10 min at −20°C or lysed for immunoblot and IP. Transfection was also stable after 48 and 72 h (Figure S3).

Immunoprecipitation and Mass Spectrometry

Exogenous TMX2 was immunoprecipitated after transfection in HEK293T cells. Initially, 15 μL EZview Red Anti-c-Myc Affinity Gel beads (E6654, Sigma Aldrich) were washed with non-denaturing TNE-1% lysis buffer (50mM Tris [pH 7.6] + 100mM NaCl + 50mM NaF + 1% NP-40 + 1mM EDTA + protease inhibitor tab; Roche). TMX2-transfected and control Lac-Myc-transfected HEK293T cells in 10 cm Petri dishes were transferred on ice, washed with 1× dPBS (Dulbecco's Phosphate-Buffered Saline), and lysed with 800 μL TNE-1% lysis buffer. To test transfection efficiency and localization, each dish contained a 24 mm coverslip, which was subsequently fixated and immunostained before the addition of the lysis buffer. Lysates were incubated on ice for 10 min and centrifuged at 10,000× g for 10 min at 4°C. The supernatant was added to the washed beads and incubated overnight under agitation at 4°C. After washing 3 times with TNE-1% lysis buffer and centrifugation at 1,000× g for 15 s at 4°C, bead pellets were subjected to a mass spectrometry (MS) preparation as described.[32] Protein Mascot scores and numbers of unique peptides were taken directly from the Mascot output and reported. Only hits with a Mascot score higher than 40 were taken into account for analysis.

Mitochondrial Respiration and Glycolysis Determination

Bioenergetics profiles of human primary skin fibroblasts were generated in real time with a Seahorse XF24 Extracellular Flux Analyzer (Agilent Technologies) as previously described.[33] Fibroblasts were seeded on a Seahorse XF-24 plate at a density of 6 × 10^4 cells per well and grown overnight in DMEM with serum at 37°C, 5% CO_2. This density ensures a proportional response to the uncoupler FCCP [Carbonyl cyanide 4-(trifluoromethoxy)phenylhydrazone] with cell number, and resulted in confluent cultures, in which cell replication was further prevented by contact inhibition. On the experimental day, the medium was changed to unbuffered DMEM (XF Assay Medium – Agilent Technologies) supplemented with 5 mM glucose and 1 mM sodium pyruvate, and it was incubated for 1 h at 37°C in the absence of CO_2. Medium and reagent acidity was adjusted to pH 7.4 on the day of the assay, according to the manufacturer's procedure. Mitochondrial respiration was measured as the oxygen consumption rate (OCR), and glycolysis was measured as the extracellular acidification rate (ECAR). After three baseline measurements for the OCR, cells were sequentially challenged with injections of mitochondrial toxins: 0.5 μM oligomycin (ATP synthase inhibitor), 1 μM FCCP (mitochondrial respiration uncoupler), 0.5 μM rotenone (complex I inhibitor), and 0.5 μM antimycin (complex III inhibitor).

For galactose experiments, cells were cultured in galactose 10 mM, 10% FCS, 2 mM glutamine, 5 mM HEPES, and 1% penicillin-streptomycin medium for three days before the bioenergetics assay.[33]

A minimum of two Seahorse replicates were performed for each fibroblast line. In each replicate, we used six wells for each line. In each run, we always used six wells for a reference primary fibroblast line with highly characterized bioenergetics behavior. We used three reference lines that were available at the Erasmus MC institute.[33]

Basal respiration was defined as the average OCR values at baseline. Respiration dedicated to ATP production was calculated as the difference between basal respiration and the respiration measured after oligomycin injection. Reserve capacity was calculated as the difference between the maximal respiration (the average OCR of the three measurements after the FCCP injection) and basal respiration. The rotenone-dependent respiration parameter was calculated as the difference between the maximal respiration value and the average OCR values obtained after the rotenone injection and was used to evaluate the activity of mitochondrial complex I. Basal glycolysis was defined as the average of the three baseline ECAR measurements, and the increase in glycolysis after blocking ATP synthase was indicated as oligomycin stimulated glycolysis.

TMX2 Redox State Assay

HEK293T cells were transfected during 24 h with plasmid DNA producing Myc-tagged β-lactamase control protein (Lac-Myc) and wild-type (TMX2) or variant TMX2 (p.Cys170Gly, p.Arg53Cys, and p.Arg231Trp) in a 6-well plate. Afterward, cells were treated with different ER-stress inducers, oxidants, and/or reductants at 37°C with 5% CO2, according to Matsuo et al.:[34] 6 h with 0.5 μg/mL brefeldin A (BFA; Cayman Chemical CAS 20350-15-6, 20 mg/mL stock in DMSO), 6 h with 5 μM thapsigargin (TG; Sigma T9033, 1mM stock in DMSO), 6 h with 10 μg/mL tunicamycin (TM; Sigma T7765, 1mg/mL stock in DMSO), 10 min with 5 mM DL-Dithiothreitol (DTT; Fluka CAS 3483-12-3, 100 mM stock in MilliQ sterile water), or 10 min with 200 μM hydrogen peroxide H_2O_2 (Merck, 822287). Free thiol groups were alkylated by washing and 10 min of incubating the cells with ice-cold 1× dPBS (Sigma Aldrich) supplemented with 20 mM N-ethylmaleimide (NEM; Sigma, E3876-5G) and 4× Laemmli buffer (3:1) before storage at

−20°C. Total protein concentrations were determined by a BCA (bicinchoninic acid) protocol with Varioskan LUX multimode microplate reader (Thermo Fisher Scientific). Equal protein concentrations were loaded onto a 4%–15% Criterion TGX Stain-Free Protein Gel (Bio-Rad Laboratories). Proteins were separated in a non-reducing SDS-PAGE with a Criterion Cell geltank (Bio-Rad Laboratories) at 100V for 1 h 40 min in Tris-Glycine-SDS running buffer. Proteins were transferred by wet blotting to a nitrocellulose membrane (Amersham Protran 0.45 NC, GE Healthcare Life Sciences) at 100V for 1 h at 4°C or alternatively on a Trans-Blot Turbo 0.2 μm nitrocellulose membrane (Bio-Rad Laboratories) at 25V, 1.5A for 20 min in a Trans-Blot Turbo transfer system (Bio-Rad Laboratories). After antibody incubation, bands were detected with a fluorescent-based approach on the Odyssey Infrared Imager (LI-COR Biosciences). Densitometry analysis to determine dimer/monomer ratios was performed in Odyssey 3.0 Software or Image Studio Lite Version 5.2.

Statistics

Statistical tests were performed with GraphPad 8 and are specified in the legends of the experiments.

Results

Clinical Overview

The clinical features observed in all 14 affected individuals, in whom we detected *TMX2* variants, have been summarized in Table 1, and full clinical and MRI descriptions are available in the Supplemental Note, Table S4, and Figure 1. Most subjects (11 of 14) were reported with microcephaly (defined as having an occipitofrontal circumference [OFC] at or below −2.5 SD for age and sex; Table 1) and, where documented, this was present at birth or at the first clinical examination. However, intra-familial discrepancy is present because only one (P5) of the two siblings of family 5 is microcephalic at adult age, whereas the other sibling (P4) has a borderline normal head circumference in the third decade of life. Two other affected individuals (P13 and P14) of family 9 and 10 did not present with microcephaly at the last examination (Table 1). With the exclusion of two individuals (P6 and P14), all have suffered from drug-resistant epilepsy, which occurred in most cases in early infancy and is characterized by apnea, epileptic spasms, myoclonic seizures, focal seizures with or without secondary generalization, generalized tonic clonic (GTC) seizures, and, in one case, possible diaphragmatic myoclonia. Three affected individuals of the cohort died during infancy, two of them of severe epilepsy in the early postnatal period. The brain imaging of these two is strikingly similar (Figure 1, P1 and P10) and resembles a congenital viral (CMV) infection because of the presence of, in addition to diffuse bilateral polymicrogyria (PMG), reduced central white matter volume, the abnormal appearance of the periventricular borders, and the existence of an occipital pseudocyst. In both cases, no infection was documented, and brain pathology excluded the presence of inflammatory signs. All subjects but one (family 10, P14) who survived beyond infancy present with severe developmental delay (Table 1), progressing to profound intellectual disability, cerebral palsy with absent ambulation and lack of speech, and/or a progressive neurodegenerative course. No additional extra-CNS (central nervous system) malformations or health issues were observed, except for the expected complications of the underlying brain pathology. Metabolic screening performed in most subjects did not reveal abnormalities of intermediate or energy metabolism. Two individuals (P4 and P5) have been followed into their third decade; they both showed signs of regression, including loss of motor skills, severely impaired cognitive skills, and no speech development.

Structural brain abnormalities were detected in almost all the subjects undergoing MRI. In seven of the twelve affected individuals who received MRI (Figure 1), a cortical malformation has been documented. Diffuse PMG (small and an excessive number of gyri) was observed in five individuals (Figure 1, P1, P2, P3, P10, and P12), whereas the two siblings from family 5 showed diffuse pachygyric (thickened and smooth) cortex (Figure 1, P6 and P7). The brain imaging of these latter siblings had been reported in the supplemental data from a cohort of undiagnosed individuals with malformations of cortical development.[24] In three other individuals (from families 4 and 6), brain imaging showed (progressive) global cerebral atrophy. The two remaining affected individuals showed an MRI with no cortical malformation (P14) or a hemihypertrophy with frontal dysgyria (P13). No brain imaging was performed in individual P8 (family 6) or individual P11 (family 8).

Brain Pathology of Affected Individuals (P1 and P10)

At autopsy of individual P1 (day 14 postpartum), the head circumference was 34 cm (−2 SD), and the brain weight was 316 g (normal weight at term: 400–450 g). Macroscopically, the brain surface was polymicrogyric; the temporal regions were the least affected (Figures 2A and 2B).

Evaluation of H&E stained sections of the frontal, parietal, temporal, and occipital cortex showed extensive unlayered polymicrogyria throughout the sampled cortical sections (Figures 2E and 2F). Undulating bands of neurons extended deeply in the cortex. The insular and parahippocampal region were least affected: the undulating neuronal bands extended less deep into the cortex. The hippocampus was spared. The transition from normal cortex to polymicrogyric cortex was abrupt. The molecular layer appeared fused between adjacent gyri, causing inclusions of pial vessels in the deep cortical region. Leptomeninges overlying the polymicrogyric cortex were focally thickened. Overmigration of neurons into the arachnoid space was not noted. The gray-white matter junction was blurred under affected cortical areas. The white matter was normal. Heterotopic remnants of the germinal matrix were occasionally observed in the periventricular region, and this sign is considered pathologic given that the affected individual was born at term. Telangiectatic vessels were present in the brain stem at the level of the locus coeruleus. Histologically, other brain structures and the eyes,

Table 1. Summary of *TMX2* Variants and Phenotypes

Affected Individuals	Family 1 - P1	Family 2 - P2	Family 3 -P3	Family 4 - P4	Family 4 - P5	Family 5 -P6[24]	Family 5 -P7[24]	Family 6 - P8	Family 6 - P9	Family 7 - P10	Family 8 - P11	Family 8 - P12	Family 9 - P13	Family 10 - P14
Ancestry	Dutch	Portuguese	White British	Puerto Rican	Puerto Rican	Spanish	Spanish	Arab	Arab	Dutch	Iraqi	Iraqi	Pakistani	Mexican
cDNA alteration	c.164A>C; c.391dup	c.614G>A homozygote	c.157C>T; c.757C>T	c.166G>C homozygote	c.166G>C homozygote	c.326A>G; c.691C>T	c.326A>G; c.691C>T	not tested	c.532G>A homozygote	c.164A>C; c.609_614+15del	c.184G>C homozygote	c.184G>C homozygote	c.178G>A homozygote	c.349A>G; c.691C>T
Protein alteration	p.Asp55Al; p.Leu131Profs*6	p.Arg205Gln	p.Arg53Cys; p.Arg253*	p.Gly56Arg	p.Gly56Arg	p.Asp109Gly; p.Arg231Trp	p.Asp109Gly; p.Arg231Trp	not tested	p.Ala178Thr	p.Asp55Ala; p.Ser203_ Thr204del	p.Asp62His	p.Asp62His	p.Asp60Asn	p.Ile117Val; p.Arg231Trp
Gender	male	male	female	male	female	female	male	female	female	male	male	male	female	female
Head size (OFC)	primary microcephaly (−3 SD at birth)	microcephaly (NA at birth; −4.5 SD current)	primary microcephaly (−2.5 SD at birth; −6.7 SD current)	borderline microcephaly (NA at birth; −2 SD current)	microcephaly (NA at birth; −3 SD current)	microcephaly (−2 SD at birth; −4 SD current)	microcephaly (NA at birth; −3 SD current)	undefined (0 SD at birth; later NA)	microcephaly (0 SD at birth; −5.5 SD current)	primary microcephaly (−2.5 SD at birth)	microcephaly (NA at birth; −4.5 SD current)	primary microcephaly (−2.5 SD at birth; −3.5 SD current)	normal (NA at birth; −0.5 SD current)	normal (NA at birth; −0.8 SD current)
Neurological impairment	no developmental milestones[a]	CP, no speech or ambulation	CP, no speech or ambulation	CP, no speech or ambulation	CP, no speech or ambulation	CP, no speech or ambulation	CP, no speech or ambulation	CP, no speech or ambulation	CP, no speech or ambulation	no developmental milestones[a]	no ambulation, few words	no speech or ambulation	able to walk with support, few words	IQ 62, language disorder, hyperactive behavior, able to walk
Survival/ age at last examination	deceased at 2 weeks	7 years	9 years	28 years	25 years	13 years	11 years	deceased at 6 years	1.5 years	deceased at 1 week	10 years	5 years	4.8 years	11.5 years
Epilepsy	generalized, apnea, status epilepticus	generalized, absence, spasms	generalized seizures	focal seizures	myoclonic-absence, GTC	no seizures	GTC	GTC	focal seizures	apnea, diaphragmatic myoclonia	generalized tonic, myoclonic seizures	GTC	myoclonic status epilepticus	no seizures
MRI	polymicrogyria	polymicrogyria	polymicrogyria	progressive brain atrophy	progressive brain atrophy	pachygyria	pachygyria	severe brain atrophy	severe brain atrophy	polymicrogyria	NA	polymicrogyria	hemihypertrophy and frontal dysgyria	normal
Brain autopsy	unlayered polymicrogyria and complete cortical disorganization	NA	NA	NA	NA	NA	NA	NA	NA	diffuse polymicrogyria and cobblestone-like malformation	NA	NA	NA	NA

Microcephaly is defined as an OFC ≤ -2.5 SD. Abbreviations are as follows: CP = signs of cerebral palsy; NA = not assessed or not available; OFC = occipitofrontal circumference; SD = standard deviations; and GTC = generalized tonic clonic seizures.
[a]These individuals passed away soon after birth.

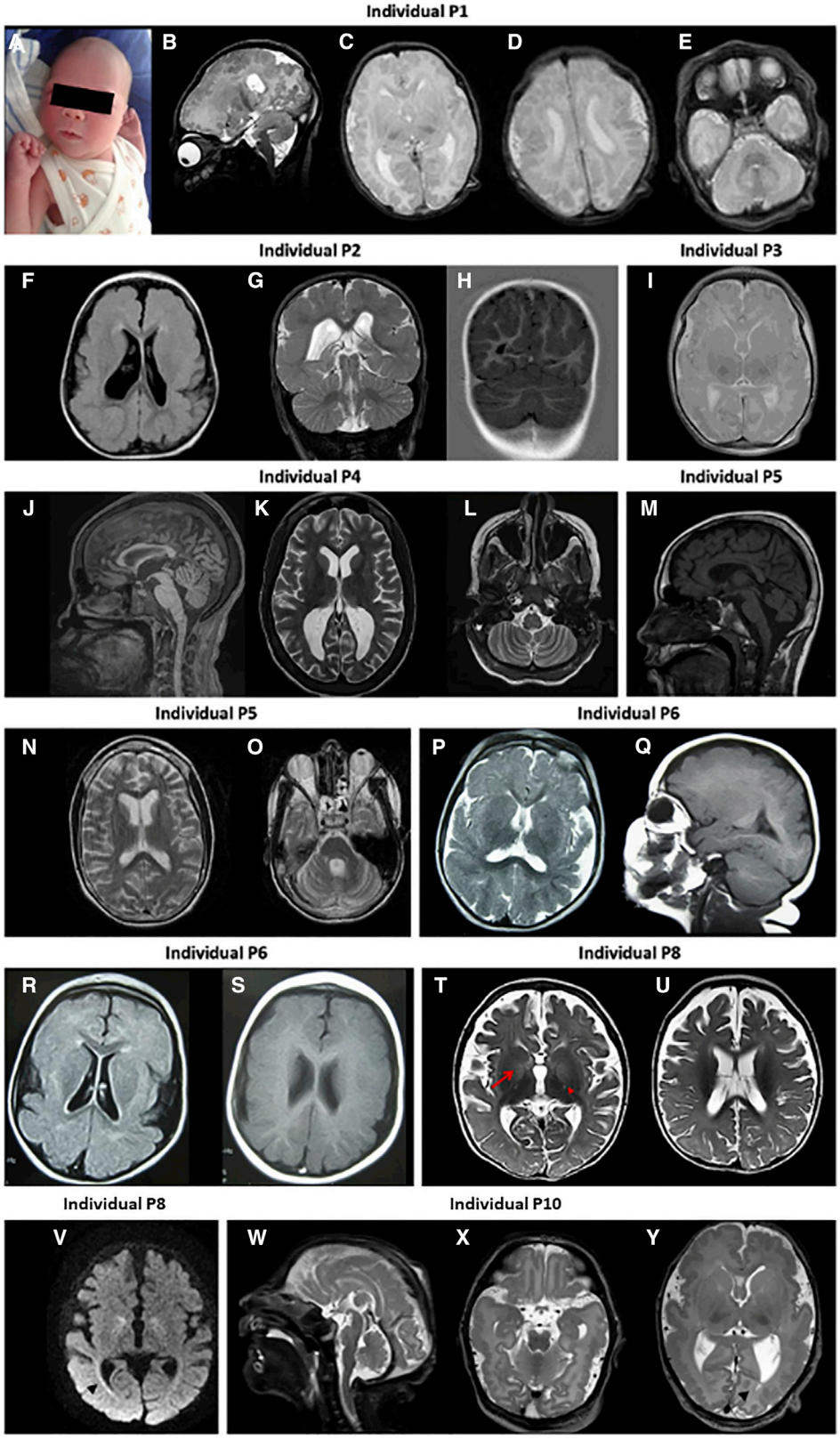

Figure 1. Features and Brain MRI of Individuals with *TMX2* Variants

P indicates the code of the probands as used in Tables 1 and S4.

(A–E) P1: affected member of family 1. (A) The photograph shows mild microcephaly and no overt dysmorphic features. The MRI scan at birth shows T2 weighted images, of (B) parasagittal plane, (C) axial at the level of basal ganglia, (D) axial at the level of parietal areas, and

(legend continued on next page)

especially the retina, appeared normal. There were no signs of mitochondrial disease or an acquired cause for the malformation, e.g., no calcifications or inflammatory cells. The basal ganglia were normal, as well as the cerebellum, which consisted of a four-layered cortex including the for-the-age appropriate external granular layer.

Brain examination of individual P10 (Figure 2C) macroscopically showed a polymicrogyric cortex of the occipital lobes, but microscopically the whole cerebral cortex was polymicrogyric, with diffuse dyslamination, fusion of molecular layers, and blurred gray-white matter junction (Figure 2G). In contrast with P1, in the polymicrogyric areas, glioneuronal heterotopia were diffusely seen migrating over the meninges in P10's brain. In the frontal area, few calcifications were seen at the gray-white matter border, and there was some calcification of the pericallosal artery but no other evidence for (focal) infection or inflammation. The occipital ependymal layer showed interruptions and gliotic changes with some reactive macrophages. The presence of neuroglial cells migrating over the glia limitans of the pia into the arachnoid space is typical of the cobblestone malformation. However, there were no additional abnormalities, such as brainstem and cerebellar hypoplasia, common in the cobblestone malformation.[35]

Genomic and Transcriptomic Analysis

Bi-allelic *TMX2* variants compatible with autosomal-recessive inheritance were identified in 14 affected individuals from ten unrelated pedigrees by WES. Detailed information on the genomic alterations (cDNA alteration, protein alteration, gnomAD frequency, SIFT, MutationTaster, and CADD scores) are described in Table S4 and the Supplemental Results, and a schematic overview of the gene and the thirteen discovered variants can be found in Figure 3A. *TMX2* encodes an eight-exon transcript (GenBank: NM_015959.3), which is translated into a protein with 296 amino acids. To test the effect of each variant on *TMX2* mRNA expression, transcriptomic analysis was performed. RT-qPCR in skin fibroblasts from the affected newborn P1 (family 1), who had a compound-heterozygous mutation in *TMX2* (c.164A>C, p.Asp55Ala; c.391dup, p.Leu131Profs*6), showed that *TMX2* mRNA expression was much lower (nearly half-fold), compared to healthy controls (Figure 3B). To determine which of the alleles was still expressed, we performed allele-specific RT-qPCR (primers specified in Table S1). Results showed that the allele carrying the frameshift in exon 4 expressed only 2%–3% of the total amount of *TMX2* mRNA seen in healthy controls, indicating that the transcript is very likely subjected to nonsense-mediated decay (NMD) (Figure 3C). When amplifying the other allele, total *TMX2* mRNA expression was likewise reduced to approximately half, confirming our previous result (Figure 3B) and showing that the allele with the c.164A>C, p.Asp55Ala variant is normally expressed (Figure 3C).

In family 2, the proband (P2) had a homozygous *TMX2* missense change with a predicted effect on splicing in the ultimate nucleotide of exon 6 (c.614G>A, p.Arg205Gln). RT-qPCR did not show a significant decrease in the expression of *TMX2* mRNA in skin fibroblasts from the proband when compared to healthy controls (Figure 3B). However, because the variant affected the last nucleotide of an exon, we suspected there would be an effect on mRNA splicing. We used RNA-seq in combination with the Integrated Genomics Viewer (IGV) to visualize cumulative transcript reads per exon in a Sashimi plot (Figure 3D), and we calculated the amount of reads per million (Figure 3E). The c.614G>A, p.Arg205Gln variant indeed affected splicing through the introduction of a new internal splice site in exon 6, resulting in four different transcripts: regular mRNA, an alternative transcript with a loss of 11 nucleotides within exon 6, an alternative transcript with full in-frame exon 6 skipping (loss of 66 nucleotides), and mRNA with intron 6 retention (Figure 3E). This latter

(E) axial at the level of pons and cerebellum. Both the parasagittal and the two axial cerebral sections show diffuse polymicrogyria of the cortex, normal myelination, hypointensity of the thalami (left axial), and normal cerebellum.
(F–H) P2: MRI of the affected individual from family 2 at 19 months of age. (F) axial-FLAIR-, (G) coronal-T2-, and (H) coronal-inversion-recovery-weighted images all showing bilateral diffuse thickened cortex that extends through frontal, parietal, and occipital areas sparing the cerebellum, and resembles polymicrogyria. The lateral ventricles are enlarged and asymmetric; the periventricular white matter volume is strongly reduced.
(I) P3: axial T2 weighted image of the affected child of family 3 at birth; it shows diffuse bilateral polymicrogyria of the cortex, mild dilatation of the posterior horns of the lateral ventricles, and delayed myelination.
(J–L) P4 and (M–O) P5: affected siblings of family 4 at the age of 12 (P4) and 23 years (P5); respectively, (J and M) sagittal T1- and (K and N) axial T2-weighted images at the level of basal ganglia and (L and O) the cerebellum, showing thin corpus callosum, loss of periventricular white matter and volume of thalami, deep cerebral sulci, and mild cerebellar atrophy. No cortical malformation is present.
(P–S) P6 is the index individual of family 5. (P) Axial T2 and (Q) parasagittal T1 images showing abnormally thick cortex and atrophic thalami; in (Q), the frontal cortex looks pachygyric. (R) Axial T2-FLAIR- and (S) axial T1-weighted images showing diffusely thickened cortex, most prominent in parietal areas and moderately enlarged lateral ventricles.
(T–V) P9: the affected proband of family 6 at the age of 11 months. Axial T2-weighted images (T and U) showing brain atrophic changes with bilateral pallidus (red arrow) and posterior limb of the internal capsule (red arrowhead) T2 high signal intensity, as well as significant delayed myelination. Globi pallidi are severely atrophic. (V) Abnormalities of both globi pallidi, posterior limb of the internal capsules, optic radiations (black arrowhead), and brainstem tract (not shown) are also noted on DWI and confirmed by ADC map (not shown), indicating restricted diffusion.
(W–Y) P10: MRI at birth of the proband from family 7. (W) Midsagittal and (X and Y) axial T2-weighted images. (W) Mild hypoplasia of the pons, thin corpus callosum. (X) Hypoplastic cerebral peduncles and bilateral abnormal cortex with polymicrogyric appearance. (Y) Diffuse bilateral polymicrogyria, enlarged lateral ventricles with pseudocyst in the left occipital horn (black arrowhead), and white matter loss; the combination includes the pseudocyst that is typically seen in CMV infections.

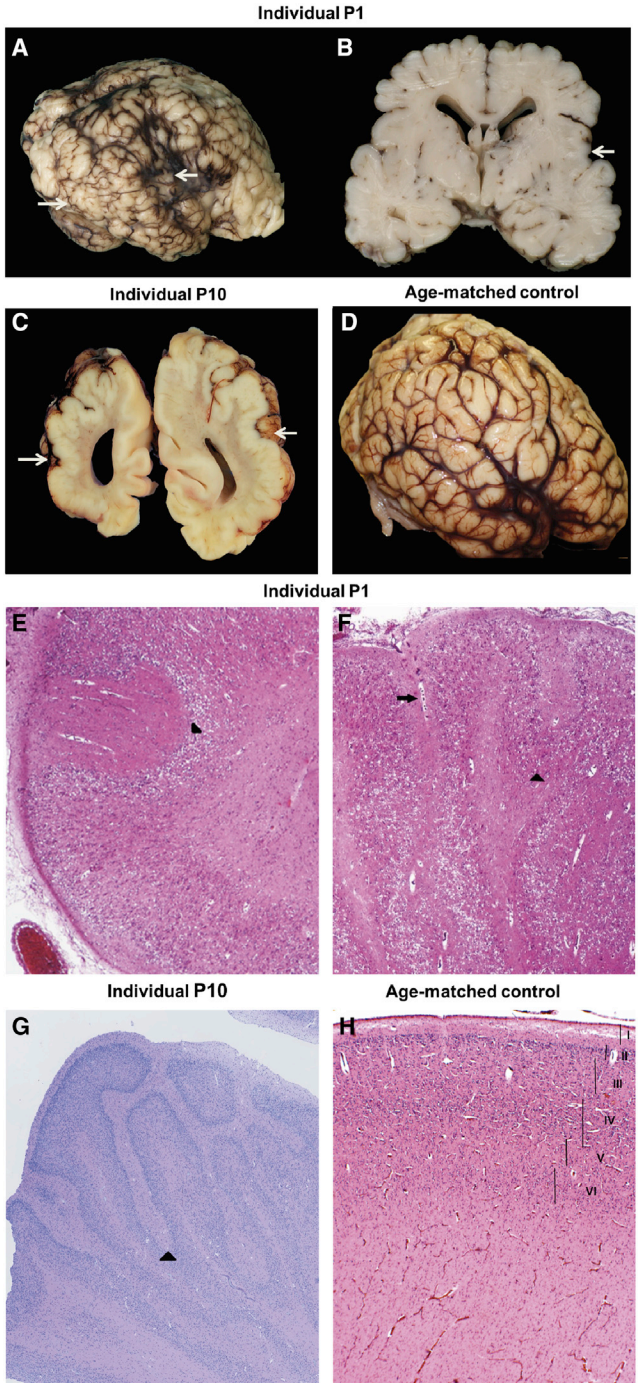

Figure 2. Brain Pathology of Individuals with *TMX2* Variants
Panels (A–C) and (E–G) depict affected individuals; panels D and H depict age-matched controls.
Upper panel: macroscopic brain appearance of P1 (A and B) and P10 (C). A sagittal view (A) and coronal section (B) show an excessive amount of diffuse and bilateral small gyri (polymicrogyria) of the cerebral cortex (most affected areas indicated by white arrows), compared to control brain (D). (C) A coronal section through the posterior parts of the brain shows asymmetric hemispheres and bilateral polymicrogyria, especially in the occipital lobes (white arrow). The image of the normal neonatal age-matched brain (40GW) shows normal size and number of gyri and sulci (lateral view of the right hemisphere) (D).
Lower panel: Histological sections of individuals P1 (E and F), P10 (G), and age-matched control brain cortex (H) show the absence of normal cortical layers in affected individuals, with bands of neurons laying perpendicular to the cortical surface in E, F, and G. Undulating bands of neurons (arrow heads), entrapped pial vessels mimicking fusion of the cortical layer (arrow), and thickened leptomeninges are compatible with (unlayered) polymicrogyria (E: H&E, 10x, F: H&E, 5x, G: Lugol-PAS stain, 3x). A control histological section of the frontal dorsolateral telencephalic gyrus of the neonatal age-matched brain (H: H&E 5x) shows the regular organization of the six-layered neonatal neocortex, parallel to the pia surface.

transcript is also present at a low level in healthy controls. Individual reads of each transcript are shown in Figure S1.

In family 3, individual P3 was found to have a combination, similar to the variants in individual P1, of a missense change in exon 1 (c.157C>T, p.Arg53Cys; which is nearby the p.Asp55Ala of P1) together with a nonsense variant leading to a premature stop codon in the last exon of *TMX2* (c.757C>T, p.Arg253*). The effect of the variants on *TMX2* transcription in skin fibroblasts was tested. RT-qPCR showed a mean decreased level of *TMX2* mRNA expression by 23%, potentially indicating that the premature termination codon in the last exon of the transcript partially escapes nonsense-mediated decay because it is less than 50 to 55 nucleotides from the stop codon at the 3′ end (for *TMX2* nt836-891) (Figure 3B).[36]

For families 4 to 10, no materials were available to test the transcriptional effect of each variant. However, considering lethality in *Tmx2* null mice, residual *TMX2* transcript can be anticipated as originating from the missense alleles and/or the allele having created a new splice acceptor site (P10).

Gene Ontology (GO) Analysis of Differentially Expressed Genes in *TMX2* Pathogenic Variants

Our data clearly indicate that bi-allelic *TMX2* variants lead to reduced *TMX2* expression, therefore acting as loss-of-function (LoF) variants (Figure 3). Compared to other TMX family members, only *TMX2* is expressed steadily from week 8 throughout fetal brain development, even increasing during postnatal life (information about mRNA expression during human brain development was retrieved from the Allen Human Brain Atlas (see Web Resources); Figure S3). We therefore considered the *TMX2* variants as probably explanatory for the early neurological manifestation and decided to investigate their effect in detail.

We performed analysis of RNA-seq data from cultured skin fibroblasts of two affected individuals (P1 and P2) in parallel with three age- and gender-matched controls and studied which pathways were deregulated.

Functional Annotation Clustering Analysis

Functional annotation clustering analysis of the top 1,000 significant differentially expressed genes (DEGs) ($p < 0.05$) by DAVID (v6.8) ranked the top cluster of genes as those associated with post-translational modifications, i.e., intramolecular or intermolecular disulfide bond formation (annotation cluster 1: disulfide bond, $p = 9.9 \times 10^{-24}$)

Please cite this article in press as: Vandervore et al., TMX2 Is a Crucial Regulator of Cellular Redox State, and Its Dysfunction Causes Severe Brain Developmental Abnormalities, The American Journal of Human Genetics (2019), https://doi.org/10.1016/j.ajhg.2019.10.009

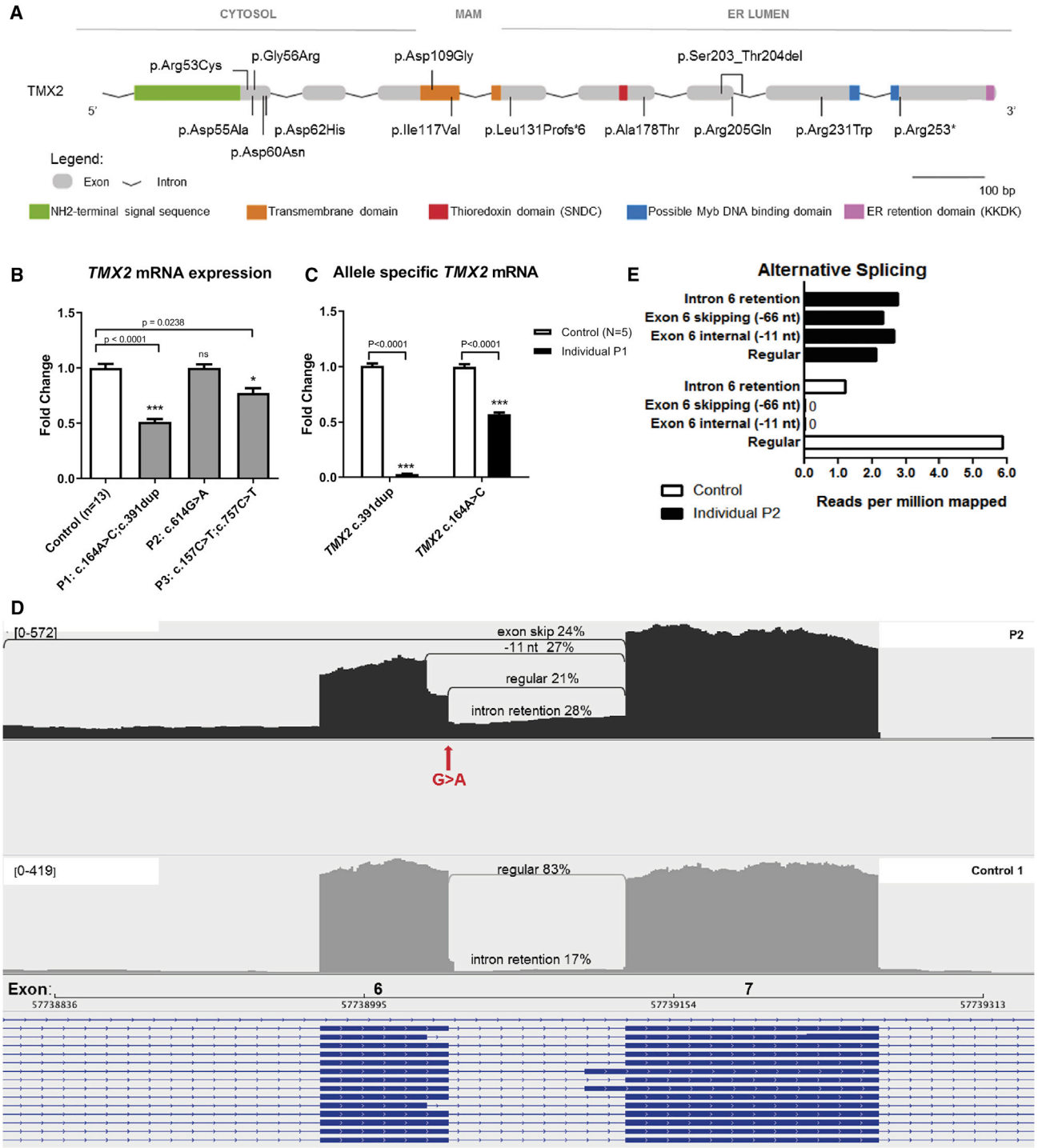

Figure 3. Genomic and Transcriptomic Analysis of *TMX2* Variants

(A) A schematic overview of *TMX2,* protein domains, and the discovered variants in affected individuals (GSDS 2.0).

(B) Levels of expressed *TMX2* messenger RNA in individuals P1, P2, and P3. Ct values were normalized with two housekeeping genes, *CLK2* and *RNF111* (ΔΔ CT relative to control [n = 2]). Data are represented as the mean ± SEM. Statistical two-tailed unpaired t tests were performed with a confidence interval of 95%.

(C) Allele-specific qPCR of individual P1. Ct values were normalized with two housekeeping genes, *CLK2* and *RNF111* (ΔΔ CT relative to control [n = 4]). Data are represented as the mean ± SEM. Statistical two-tailed unpaired t tests were performed with a confidence interval of 95%.

(D) Aberrant splicing of the P2 and control *TMX2* alleles. This is a graphic illustration (adapted from an IGV Sashimi plot) of the percentage of *TMX2* transcripts in RNA-seq data of total RNA of individual P2 and one control individual. Percentages are calculated for each transcript compared to the total *TMX2* (wild type and alternative) transcript reads (GRCh38).

(legend continued on next page)

and N-linked glycosylation (annotation cluster 1: glycoprotein, $p = 2.1 \times 10^{-28}$, and glycosylation site: N-linked, $p = 2.5 \times 10^{-27}$) (Figure 4A). From this cluster of genes, 24 disulfide-containing genes were subtracted as being the highest deregulated of this cluster in cells from affected individuals; they had a false discovery rate (FDR) lower than 0.05 (Figure 4B). Stringent filtering (FDR < 0.01) without clustering uncovered 37 differentially expressed genes, of which five, i.e., *CXCL5* (OMIM: 600324),[37] *DAPK1* (OMIM: 600831),[38] *HGF* (OMIM: 142409),[39] *LTBP1* (OMIM: 150390), [40] and *CES1* (OMIM: 114835),[41] are indirectly controlled by the UPR or regulate expression of UPR markers. Interestingly, the second highest deregulated gene, *LTBP1*, encodes a known folding substrate for another PDI protein, ERp46, also known as TXNDC5.[42,43] Although it has been suggested that most PDIs show substrate specificity,[2] LTBP1 could also be a substrate of TMX2 or TMX2 might affect TXNDC5-mediated folding.

The second most significant functional annotation cluster ranks genes that have a transmembrane domain (enrichment score = 9.43), and a third most significant cluster contains genes encoding proteins involved in synaptic function, specifically located at the postsynaptic membrane (enrichment Score = 4.63). This latter membrane is enriched with receptors and ion channels essential for the interaction with neurotransmitters. Interestingly, another cluster mentions the deregulation of calcium ion binding (annotation cluster 6, enrichment score = 3.16).

Ingenuity Pathway Analysis

Ingenuity pathway analysis (IPA) of the same differentially expressed genes in cells from the two probands ($p < 0.05$), taking into account the logarithmic fold change (LogFC) of each gene, was used to calculate the most affected biological functions and disease networks (Figure 4C). Only activation *Z* scores in the 90% confidence interval were considered to be significant ($Z[-\infty,-1.65]$ and $Z[1.65, +\infty]$). Interestingly, this analysis showed that two key IPA categories, i.e., "Nervous System Development and Function" and "Cellular Growth, Proliferation and Survival," were inhibited in *TMX2*-variant affected individuals (blue bars in Figure 4C). The most significant inhibited function was "quantity of neurons" ($Z = -2.864$), with a decreased outgrowth of cells ($Z = -2.818$), specifically neurons ($Z = -2.594$) and neurites ($Z = -2.46$), all related to processes affected in microcephaly. Consequently, transcripts related to learning ability ($Z = -2.356$) and cognition function ($Z = -2.257$) were also shown to be potentially decreased in cells from affected individuals. Moreover, besides the development of neurons ($Z = -1.955$), the differentiation of neurons ($Z = -1.812$) was highly inhibited. Lastly, overall cell survival ($Z = -1.785$) and viability ($Z = -2.016$) were decreased. When looking at the most activated biological functions or associated diseases, seizures ($Z = 2.712$) and seizure disorder ($Z = 2.819$) are the most significant activated features (red bars in Figure 4C).

Proteomics Analysis of Exogenous TMX2

In light of the effect of *TMX2* variants on transcriptome, specifically on disulfide bond formation, we wondered whether TMX2 functions as an oxidoreductase and/or chaperone in protein folding. A transfection protocol was optimized in HEK293T cells with a Myc-tagged vector containing full-length *TMX2* sequence (p.CMV6.TMX2-Myc/DKK) and a Myc-tagged β-lactamase vector as negative control (pcDNA3.1/Myc-His (-)/LacZ). Immunocytochemistry of exogenous TMX2 localized the protein to the MAM through co-localization with the marker calnexin (CNX) (Figure S4A) and in the vicinity of the mitochondria, visualized by mitochondrial marker HSP60 (Figure S4B). Next, we aimed at the identification of the TMX2 interacting proteins by performing MS-based proteomics of co-precipitated proteins. A 24 h overexpression of Myc-tagged *TMX2*, followed by IP and LC-MS/MS, reveals 71 unique peptides as putative interactors. The list of reproducible co-precipitated proteins is shown in Table S5 and visualized with Cytoscape String App according to pathway involvement in Figure 5A. An interesting observation was that TMX2 physically interacts with MAM marker CNX, which is a calcium-binding protein-folding chaperone. Other PDIs, e.g., TMX1,[2] TMX4,[6] and ERp57,[2] have also been shown to bind with CNX. Binding was reciprocally confirmed after IP of CNX and detection of Myc-tagged TMX2 on immunoblots (Figure 5B). Besides CNX, multiple other protein-folding regulators and ER chaperones, including co-chaperones of the HSP70 family DNAJA2(HSP40) and BCL2-associated athanogene 2(BAG2), chaperonin containing TCP1 subunit 5 (CCT5), translocon-associated protein/TRAP subunit alpha (SSR1), and the N-glycosylation regulators glucosidase II alpha subunit (GANAB) and Dolichyl-diphospho-oligosaccharide-protein glycosyltransferase complex (OST complex: RPN2, DDOST, STT3B, MLEC),[44] were interacting with TMX2 (Figure 5, dark blue).;

Furthermore, besides CNX, TMX2 bound other key regulators, i.e., Ca^{2+}-binding proteins (RCN2, HAX1, and SSR1) and Ca^{2+}-ion channels located at the MAM or mitochondrial membrane (ATP2A2/SERCA2 and VDAC1) (Figure 5A, light blue), of calcium homeostasis. TMX2 also binds Erlin-2, which directly regulates inositol 1,4,5-trisphosphate Ca^{2+} receptor degradation. These calcium receptors and channels are necessary for mitochondrial bioenergetics. SERCA2, like CNX, is a main interactor of some PDI members (including TMX1[7] and

(E) Aberrant splicing of the P2 and control *TMX2* alleles. Aligned, uniquely mapped reads in the exon 5–7 region of *TMX2* were quantified (reads per million) by IGV 2.3.26. Three distinct alternative species of *TMX2* transcript were identified, consistent with intron 6 retention, exon 6 skipping, and exon 6 internal splice site usages; the latter two were found only from the P2 allele. Total uniquely mapped reads for the control and individual P2 were 64,745,034 and 54,200,090, respectively.

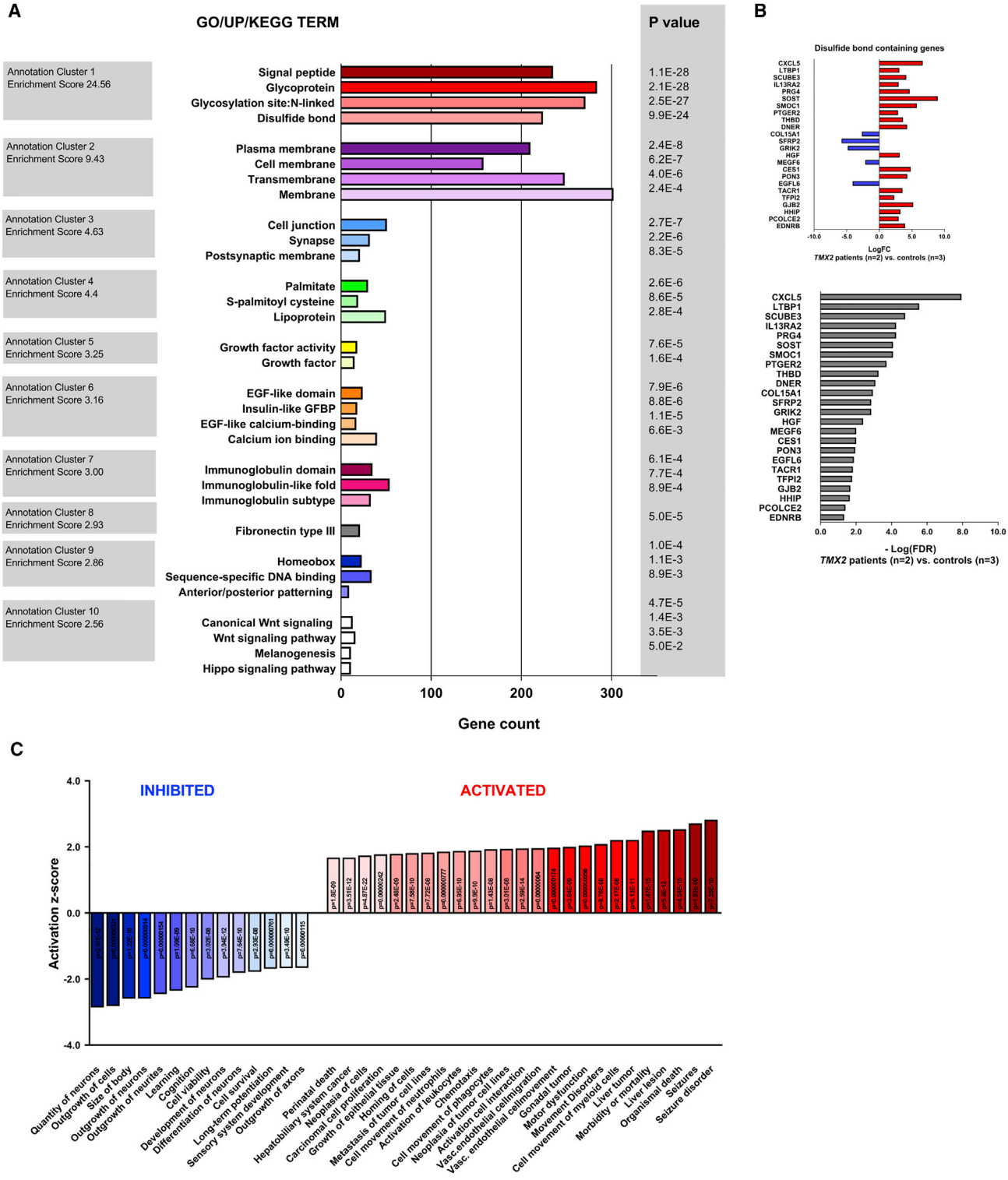

Figure 4. Gene Ontology (GO) Analysis of Differentially Expressed Genes in *TMX2* Variants

(A) DAVID Functional Annotation Clustering (FAC) analysis of the top 1,000 differentially expressed genes (DEGs) obtained by comparison of two *TMX2*-variant affected individuals versus three age- and gender-matched control RNA samples (p value < 0.05).

(B) Upper panel: LogFC of all differentially expressed disulfide-bond-associated genes in *TMX2*-variant affected individuals with an FDR < 0.05; lower panel: -Log(FDR) of these genes (-log(FDR) < 1.3).

(C) Ingenuity Pathway Analysis (IPA) was performed to determine activated and inhibited biological functions downstream of the differentially expressed genes in *TMX2*-variant affected individuals. Stringency was determined with a 90% confidence interval by only considering activation *Z* scores higher than 1.65 (activation) or lower than −1.65 (inhibition). Individual p values of each function are mentioned within the bars and were always lower than 10^{-6}.

Abbreviations are as follows: GO = gene ontology; UP = UniProtKB; FDR = false discovery rate; FC = fold change; and KEGG = Kyoto Encyclopedia of Genes and Genomes.

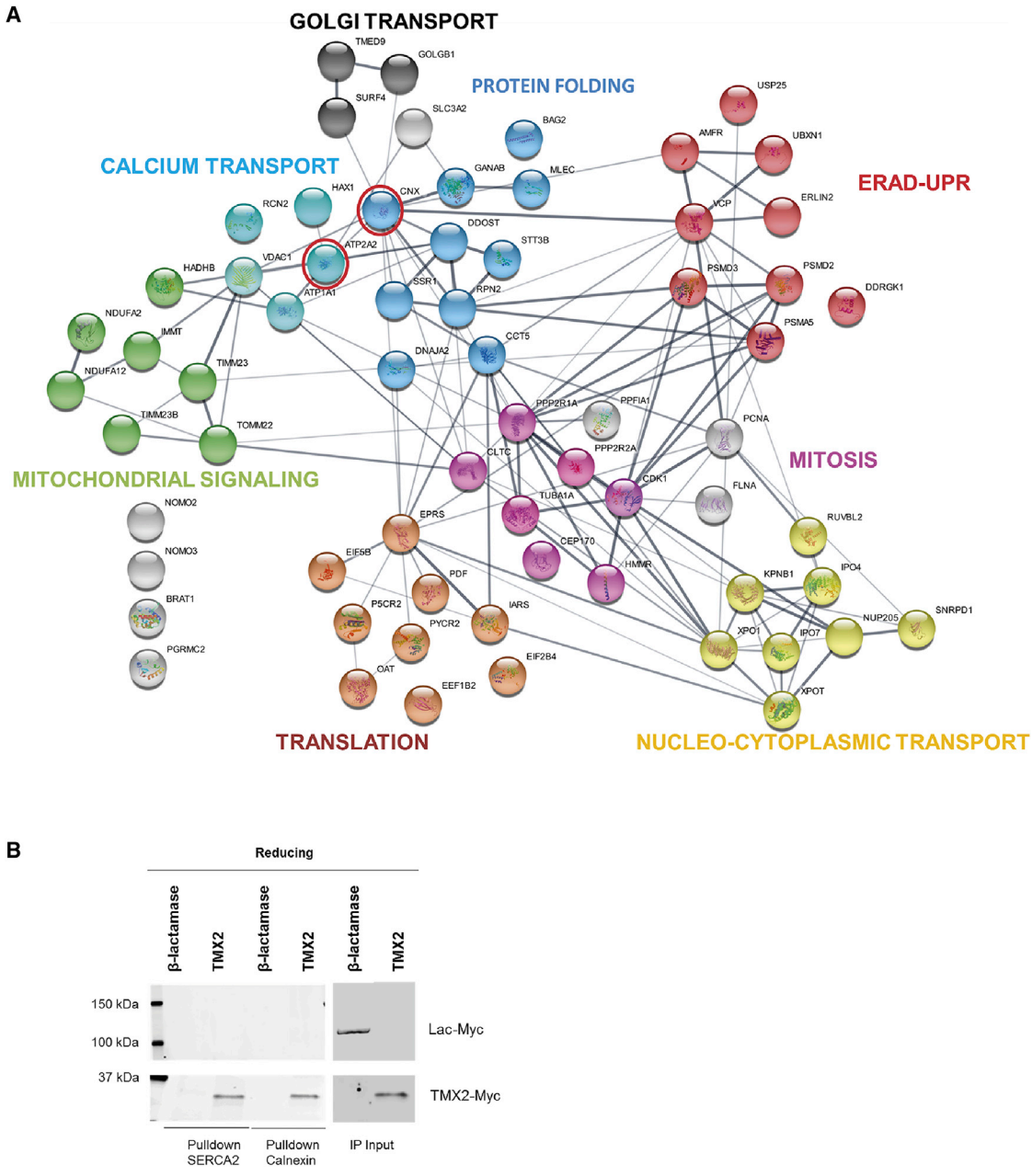

Figure 5. Proteomics Analysis of Exogenous TMX2 Interacting Proteins

(A) HEK293T cells were transfected with Myc-tagged TMX2 or negative control β-lactamase for 24 h, followed by immunoprecipitation (IP) with αMyc antibody and LC-MS/MS on bead pellets. Detected proteins interacting with TMX2-Myc but not with Lac-Myc were filtered on the basis of average Mascot score in n = 4 experiments (significant if higher than 40). Cytoscape String App visualized all 71 proteins reproducibly and selectively interacting with TMX2 according to pathway involvement (dark blue = protein folding, light blue = calcium homeostasis, red = ER-associated degradation (ERAD) and unfolded protein response (UPR), green = mitochondrial signaling, pink = mitosis, orange = translation, yellow = nucleus transport, black = golgi transport, and grey = unassigned). Known PDI interactors Calnexin and SERCA2 were found in the top 10 highest interactions and are circled in red.

(B) HEK293T cells were transfected with Myc-tagged TMX2 or negative control β-lactamase for 24 h, followed by reciprocal immunoprecipitation of SERCA2 (mouse monoclonal anti-SERCA2 ATPase ab2861) and Calnexin (monoclonal rabbit anti-human CNX C5C9), SDS-PAGE, and detection of TMX2 with αMyc antibody. IP input is shown after a reducing immunoblot.

ERdj5[1]) and described as a key regulator of protein folding. Binding was confirmed reciprocally after IP of SERCA2 and detection of Myc-tagged TMX2 on immunoblot (Figure 5B). Proteomics data also indicate physical interaction of TMX2 with mitochondrial outer and inner membrane complex components (Figure 5A, green), e.g., the mitochondrial contact site and cristae organizing system (MICOS, MIC60/IMMT subunit), the mitochondrial precursor protein import pathways (TOM22 and TIM23 complex),[45] and the mitochondrial membrane respiratory chain NADH dehydrogenase (complex I NDUFA2 and NDUFA12 subunits).

TMX2 also interacted with proteins, i.e., DDRGK1, a direct regulator of IRE1α-XBP1 and PERK-eIF2α-CHOP signaling,[46] regulating the UPR or the UPR-associated endoplasmic-reticulum-associated degradation (ERAD), dependent on an ubiquitin-proteasome system (UPS) (Figure 5, red), i.e., TMX2 binds with VCP-AMFR ERAD complex, Erlin-2 involved in ERAD of IP3Rs, ubiquitin-binding protein UBXN1, deubiquitinating enzyme USP25, and proteasome subunits PSMD2, PSMD3, and PSMA5. Because of these interactions, because the RNA-seq showed dysregulated genes indirectly linked to UPR signaling, and because of the role of TMX2 in protein folding, we tested the hypothesis of whether *TMX2* variants activated the UPR, specifically the IRE1α-XBP1 and PERK-eIF2α-CHOP signaling. RT-qPCR of UPR downstream mRNA markers *CHOP* and spliced *XBP1* was performed for the three available fibroblast lines derived from affected individuals and showed that aberrant TMX2 did not affect the amount of expressed s*XPB1* nor *CHOP* (data not shown). Although the RNA-seq data of affected individuals showed DEGs indirectly linked to the UPR, no direct factors of any of the three UPR pathways were found to be upregulated when *TMX2* was mutated. Hence, together these data indicate that *TMX2* pathogenic variants do not lead to constitutive UPR activation in fibroblasts from affected individuals.

Mitochondrial Bioenergetics in *TMX2* Variant Fibroblasts

PDIs and protein folding are important determinants for normal mitochondrial bioenergetics and cell survival. In view of the putative function of TMX2 at the ER-MAM-mitochondria interface, the results of RNA-seq (hinting toward a deregulated disulfide bond formation and calcium binding in cells from affected individuals) and proteomics analysis (showing binding with regulators of protein folding, ERAD, ER-mitochondrial UPR, and calcium homeostasis), we focused on mitochondrial activity and evaluated mitochondrial respiration and glycolytic activity in *TMX2* variant fibroblasts derived from three affected individuals (P1, P2, and P3) with a Seahorse Extracellular Flux Analyzer. Only P3 showed reduced basal mitochondrial activity and reduced respiration dedicated to ATP production when compared to healthy control lines. At the same time, all *TMX2* variant fibroblasts featured suppressed mitochondrial respiration upon stimulation with the mitochondrial uncoupler FCCP, with a significantly reduced reserve capacity—which reflects the bioenergetics reservoir available to counteract cellular stress—and overall decreased rotenone-dependent respiration. The latter indicates a reduced activity of mitochondrial complex I (Figures 6A and 6C). Interestingly, P1 and P2 but not P3 showed a significant increase in the glycolytic activity that was measured as lactate-dehydrogenase-mediated acidification of the medium, both in basal condition and upon stimulation with the mitochondrial ATP-synthase inhibitor oligomycin (Figures 6B and 6D), indicating that *TMX2* variant fibroblasts compensated the mitochondrial bioenergetics defects by potentiating the glycolytic pathway and glucose catabolism. Quantification of cellular ATP levels showed no differences between *TMX2*-variant affected individuals and controls (Figure S5). To identify potential mitochondrial defects silenced in glycolysis-permitting conditions, we performed the experiments also in conditions where glycolysis was inhibited by the presence of galactose, forcing cells to rely on mitochondrial respiration for ATP production. As expected, P1 and P2 failed to potentiate basal respiration and showed no significant increase of respiration dedicated to ATP production or of mitochondrial complex I activity when cultured in galactose medium, although they retained the ability to potentiate the reserve capacity (Figure 6E).

Redox State Analysis of Wild-Type and Variant TMX2

TMX2 Oxidizes and Reduces in Native Conditions

We tested whether thiol groups in TMX2 can be oxidized and reduced and thus whether TMX2 is able to form disulfides and hence be able to influence protein folding. HEK293T cells were transiently transfected with *TMX2* (Figure 7A) or β-lactamase vector (Figure 7B), and the redox state of TMX2 was monitored before and after treatment with the reducing agent DTT, the oxidant hydrogen peroxide (H_2O_2), or the ER-stress inducers brefeldin A (ER-Golgi transport blocker) (Figures 7A and B), thapsigargin (SERCA2 inhibitor), or tunicamycin (N-glycosylation inhibitor) (Figure 7C). To be able to distinguish the redox state of cysteines, cells were incubated with a cysteine alkylating reagent N-ethylmaleimide (NEM) to covalently bind reduced thiol groups (+0.125kDa/thiol) but not oxidized disulfide groups. Figure 7A, lanes 1 and 5, shows that TMX2 exists in both a reduced NEM alkylated form (~33 kDa) and an oxidized lower molecular form (~31 kDa) in native conditions. These two bands were consistently found in all of our repeat experiments with the ratios of oxidized and reduced TMX2 alternating, e.g., sometimes more reduced TMX2 (Figure 7A, lane 1), sometimes equal amount (Figure 7C, lane 1), and sometimes more oxidized TMX2. ER stress induced by BFA, tunicamycin, or thapsigargin did not alter TMX2 redox state (Figure 7A, lanes 2 and 6, and Figure 7C, lanes 2, 5, and 6) nor its protein level. DTT treatment partially shifted the redox state to a more reduced TMX2 (Figure 7A, lane 3), and TMX2 was completely reduced in the presence of β-mercaptoethanol (Figures 5B and S6), indicating that at least part of the TMX2 redox state is thiol-mediated.

TMX2 Dimerizes and Oxidative Stress Elevates the Dimer/Monomer Ratio

Surprisingly, H_2O_2-mediated oxidation of cells overexpressing TMX2 did not result in an increase of the lower oxidized TMX2 band, as we observed for PDI (PDIA1) (Figure 7A, lane 12), but it instead generated an intense TMX2-reactive extra band with higher molecular mass on immunoblot (Figure 7A, lanes 4 and 8; apparent mass ~65 kDa). Because molecular mass was double the amount of a TMX2 monomer, we hypothesize that this band represents a slower-migrating homodimer. Dimer/monomer

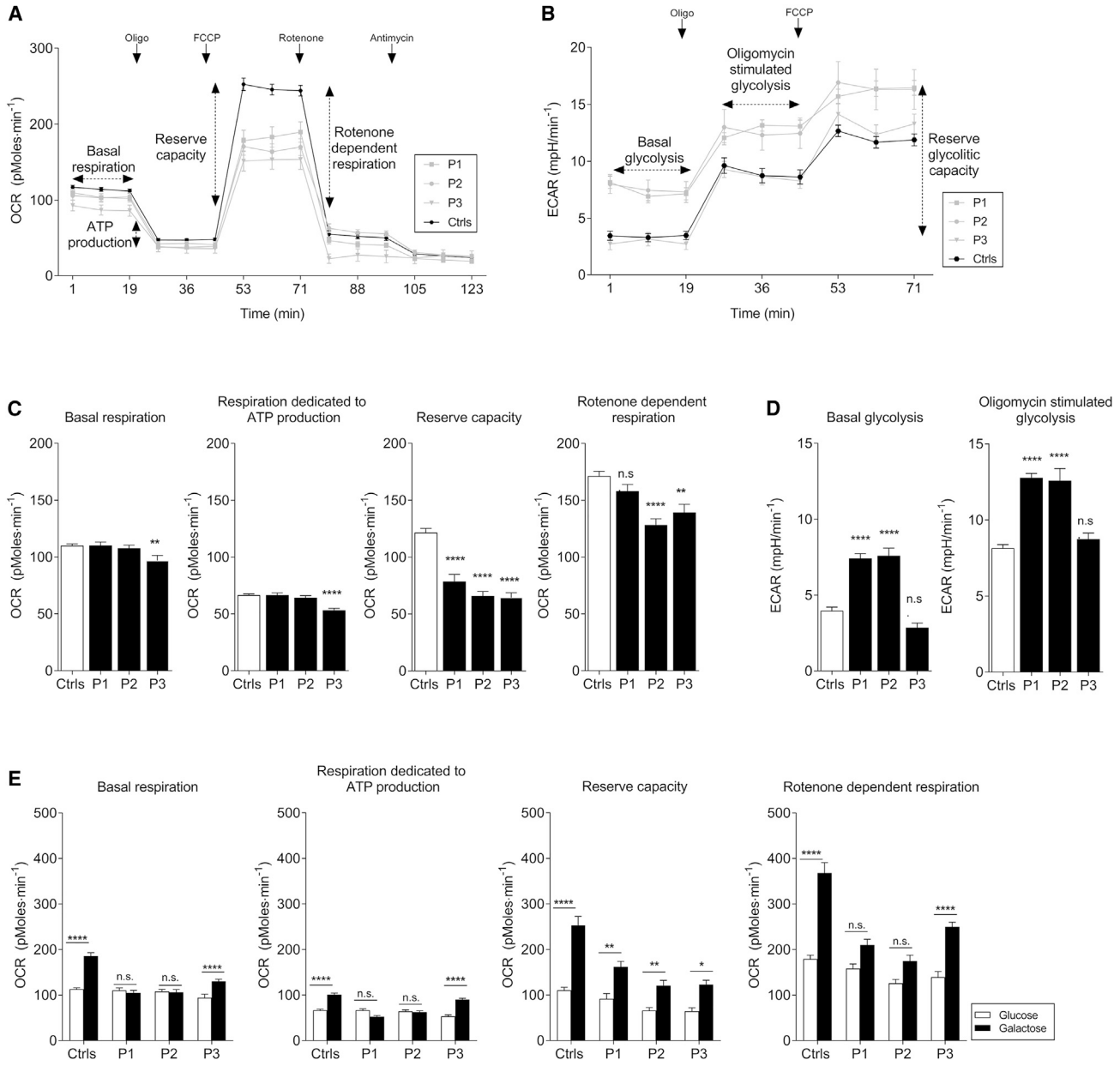

Figure 6. Bioenergetics Profiles of Skin Fibroblasts from Affected Individuals with *TMX2* Variants

(A and B) Oxygen consumption rate (OCR) (A) and extracellular acidification rate (ECAR) (B) bioenergetics profiles of fibroblasts derived from healthy controls (n = 4) and affected individuals (P1, P2, and P3). Fibroblasts were challenged with sequential administration of oligomycin to inhibit ATP synthase, FCCP to elicit maximal respiration, rotenone to inhibit complex I, and antimycin to inhibit complex III and fully block respiration. The parameters analyzed in the profiles were: basal respiration, respiration dedicated to ATP production, (measured as the difference between basal respiration and the respiration after oligomycin injection), mitochondrial reserve capacity (measured as the difference between maximum reserve capacity and basal respiration), and rotenone-sensitive respiration (which accounts for the respiration dependent on complex I), basal glycolysis, and oligomycin-stimulated glycolysis.

(C and D) Fibroblasts derived from affected individuals show significant reduction in mitochondrial reserve capacity and in the complex I activity (C) while showing a significant potentiation of glycolysis in basal condition and upon stimulation with oligomycin (D).

(E) The analysis of mitochondrial respiration in galactose medium (where glycolysis is not permitted) highlights the inability of the *TMX2* variant fibroblasts to potentiate basal mitochondrial respiration and mitochondrial complex I activity. (*$p < 0.05$, **$p < 0.01$, and ****$p < 0.0001$ by one-way ANOVA [C and D] and two-way ANOVA [E], followed by Dunnett's multiple-comparison post doc test). Graphs represent mean ± SEM.

ratios were calculated and showed up to a 200-fold increase of dimerization in an oxidative environment (Figure 7D, H_2O_2, $p = 0.0005$). The dimer was still present when SDS-PAGE was performed in reducing conditions with β-mercaptoethanol and without NEM, although the ratio of dimer/monomer was almost inverted, and the monomer represented the major band (Figure S6). These results indicated that oxidative conditions mediated by H_2O_2 induce dimerization of TMX2, and that this dimerization is at least partially mediated by disulfide bond formation.

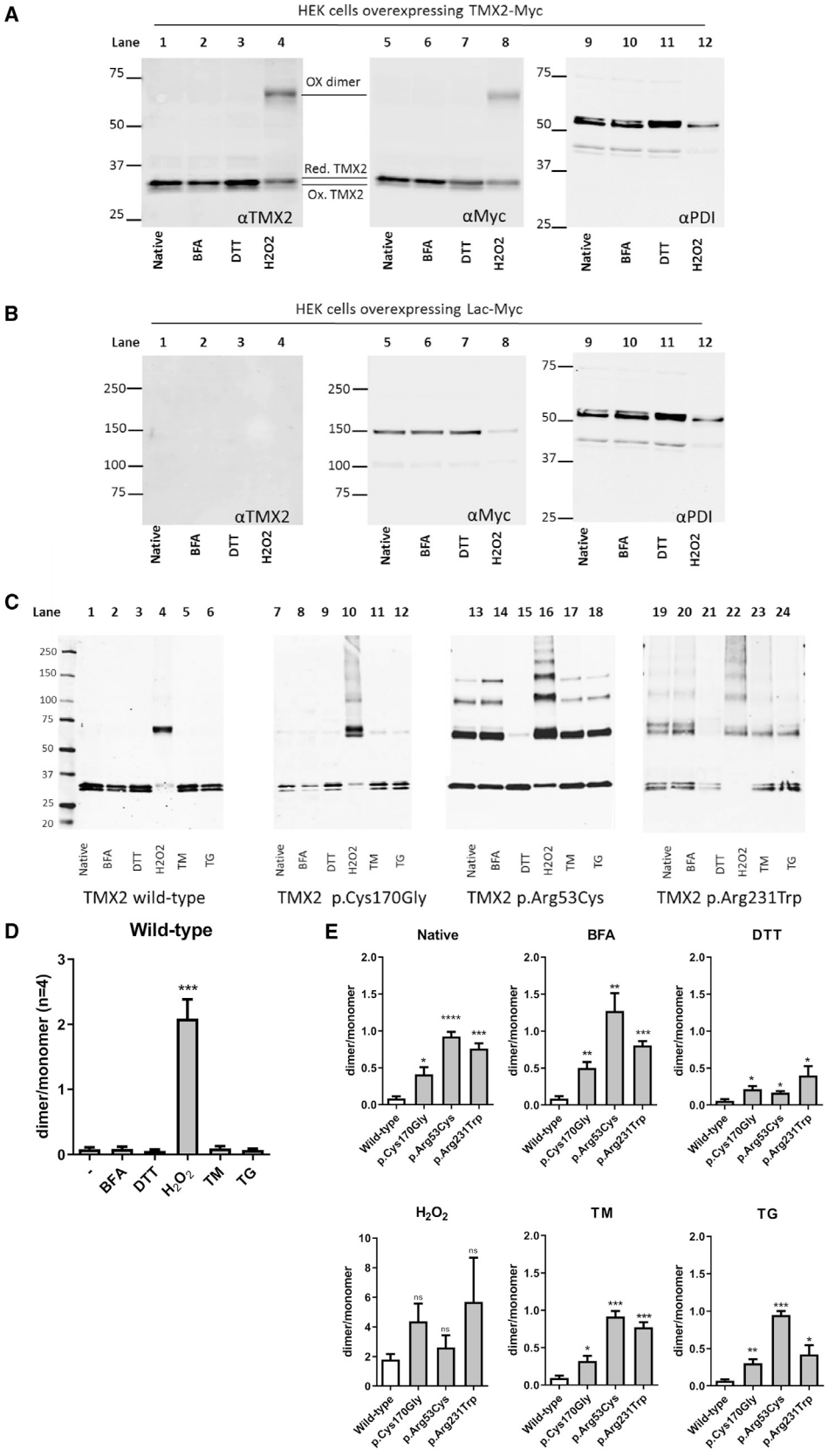

Figure 7. Redox State Assays of Wild-Type and Variant TMX2

(A and B) A non-reducing immunoblot of exogenous wild-type TMX2 versus endogenous control PDI (PDIA1) in HEK293T cells, showing that TMX2 occurs in an oxidized and reduced monomeric form, whereas during H_2O_2 treatment, a dimer is formed (OX dimer). (A) Left panel: the blot after incubation with anti-wild-type TMX2 antibodies. Middle panel: incubation with anti-Myc antibodies. Right

(legend continued on next page)

Homodimerization was confirmed through linear correlation between the observed molecular weight on blot (average 57.8 kDa, n = 18) and the calculated expected molecular weight with the method of Lambin for a gradient SDS-PAGE gel (4%–15%) (Figure S7).[47]

TMX2 Variants Highly Dimerize and Polymerize in Native and ER-Stress Conditions

We tested the effect of variants on the behavior of exogenously expressed TMX2. By *in vitro* mutagenesis, the single cysteine in the atypical thioredoxin domain was substituted with a glycine, p.Cys170Gly. Interestingly, ablation of the active cysteine in the TRX domain still permitted dimerization, and this supports the hypothesis that this dimer is not a mixed disulfide dimer of the TRX domain with another substrate. Moreover, dimerization of TMX2 was appreciated in the TRX domain variant, even under native conditions, i.e., independently of an oxidative stress, suggesting that this domain is involved in the reversibility of the TMX2 state between monomer and dimer (Figure 7E). Furthermore, oxidative stress even induced the formation of higher molecular weight polymers in the TRX domain mutant (Figure 7C, lane 10). To determine the redox state of human *TMX2* pathogenic variants under different stress conditions, we overexpressed either a *TMX2* variant located in the cytosolic domain, p.Arg53Cys, or a variant in the ER lumen domain, p.Arg231Trp (Figure 7C, lanes 13–18 and 19–24). Strikingly, the amount of TMX2 dimer was significantly higher compared to wild-type TMX2 for both variants in both native and under all stress conditions, not only H_2O_2, as quantified in Figure 7E. Dimer/monomer ratios were increased by 10-fold (1:1), whereas in wild-type TMX2 there is a ratio of 0.1:1, showing that the pathogenic variants block the protein in a dimerized state and that affected individuals might have less monomeric protein available (Figure 7E). Moreover, TMX2 with the natural variants also displayed higher levels of polymerization, as seen in the TRX mutant (apparent mass ~110 kDa and 140 kDa, observed average mass 97.1 kDa and 138.9 kDa with method of Lambin in n = 11). On the basis of the linear correlation between observed and expected mass, these bands seem to represent homotrimers and tetramers of TMX2 (Figure S7). Although the amount of dimer to monomer ratios under oxidative stress was also doubled or tripled in mutant p.Arg231Trp or p.Arg53Cys TMX2 compared to wild-type TMX2, the difference was no longer significant (Figure 7E, H_2O_2, fourth graph). DTT treatment prevented polymerization of the variants almost completely, confirming that polymerization is (at least partially) mediated by disulfide bridge formation (Figure 7E, third graph, and Figure S6). Notably, *in vitro* mutagenized Myc-tagged TMX2 was still able to bind both CNX and SERCA2 (Figure S8).

Discussion

We describe a disorder, characterized by developmental delay, microcephaly, impaired speech and ambulation, epilepsy, and cortical malformations, that has a relatively wide spectrum of severity ranging from early death to intellectual disability with mild motor impairment and resulting from recessive *TMX2* variants.

Redox regulatory proteins are enriched at the MAM of the smooth ER.[10,48] Some of these proteins interact with ER calcium-handling proteins and regulate the calcium flux into the mitochondria, a process that, in turn, influences mitochondrial membrane potential and mitochondrial respiration.[1] Thioredoxins of the PDI family regulate the cellular redox state through oxidoreductase-activity-mediated disulfide bond formation and contribute to protein folding. The PDI transmembrane ER thioredoxin-related (TMX) proteins, such as MAM-associated TMX1, seem to have dual function: on the one hand, they regulate protein folding, maintaining the redox environment of the ER and hereby preventing ER stress, and on the other hand, they regulate calcium flux in the mitochondria.[7] Besides regulating protein folding and calcium transport, thioredoxins in general are key molecules in the regulation of oxidative stress through scavenging reactive oxygen species (ROSs), such as hydrogen peroxide.[49]

TMX2 lacks the canonical oxidoreductase active C-X-X-C domain. However, its function as a folding chaperone is suggested by our data, demonstrating (1) the dysregulation of disulfide-bond- and N-glycosylation-related genes in *TMX2*-deficient fibroblasts, (2) the interaction of TMX2 with several proteins regulating protein folding and UPR, and (3) the presence of both oxidized and reduced forms in the maleimide alkylation assay. In addition, our mechanistic studies discover the function of TMX2 as a regulator of calcium homeostasis and mitochondrial bioenergetics. TMX2 localizes at the MAM,

panel: anti-PDI control protein antibodies. (B) Control experiment after expression of exogenous control β-lactamase (Lac-Myc); immunoblotting was performed with the same antibodies as in (A). Native = untreated cells; BFA = cells treated with ER stress inducer Brefeldin A; DTT = cells treated with reducing agent DL-Dithiothreitol; and H2O2 = cells treated with hydrogen peroxide.
(C) A non-reducing immunoblot with a similar experimental setup as in (A and B), but here there was also the addition of ER stress inducers Tunicamycin (TM) and Thapsigargin (TG). Redox states of TRX domain p.Cys170Gly variant (lanes 7–12) and the affected individual p.Arg53Cys variant (lanes 13–18) and p.Arg231Trp variant (lanes 19–24) were determined simultaneously. Detection was performed with anti-Myc antibody.
(D and E) Semiquantitative densitometry calculations of TMX2 dimer/monomer ratios in native, ER stress, oxidative, and reductive environments for wild-type TMX2, n = 4 immunoblots from biological replicates (D). Semiquantitative densitometry calculations of TMX2 dimer/monomer ratios in wild-type TMX2 to p.Cys170Gly, p.Arg53Cys, and p.Arg231Trp variants in native, ER stress, oxidative or reductive environment (E). Data are represented as the mean ± SEM. Statistical two-tailed unpaired t tests were performed with a confidence interval of 95% in Graphpad Prism 8 (*$p < 0.05$, **$p < 0.01$, ***$p < 0.001$, and ****$p < 0.0001$).

where it physically binds to calnexin and SERCA2, whereas *TMX2*-variant fibroblasts show decreased mitochondrial reserve capacity and lower ability to cope with oxidative stress, probably related to defective calcium flux, similarly to what was proposed for *TMX1*-deficient cells.[7] Compared to *TMX*1, *TMX2* is highly expressed in the fetal and postnatal brain. The specific *TMX2* expression in the cortex during prenatal life, together with the deleterious effect of its loss of function for human cortical development, places TMX2 as a key molecule in the ER-mitochondrial redox regulation of brain development. Although pathogenic variants in mitochondrial oxidoreductases and MAM-associated proteins have been reported as causes of pediatric neurologic disorders,[16–20] the TMX2-related disorder is a malformation of cortical development resulting from a defect in a member of the PDI family.

TMX2 is thus an important regulator of oxidative stimuli, and an intriguing aspect is its responsiveness to H_2O_2. The sensitivity of TMX proteins to H_2O_2 has received little attention, although it has been shown that their redox state dramatically changes after H_2O_2-treatment, as it happens, for example, for TMX4.[6] The hydrogen peroxide signaling molecule has long been considered to be deleterious for cellular function and a by-product of oxidoreductase reactions, because it is rapidly metabolized by catalases, glutathione-peroxidases, or peroxi-redoxins.[49] However, more recent findings highlighted the role of H_2O_2 as a physiological regulator of redox signaling (oxidative eustress), acting via reversible cysteine and methionine oxidation.[50] Additionally, H_2O_2 functions in higher concentrations as a mediator of pathophysiological signals (oxidative distress), leading to growth arrest and regulated cell death.[50] One of the main intracellular sites of H_2O_2 production is the ER.[51] Along with the activation of peroxi-redoxins as possible intermediate sensors, the role of H_2O_2 in the development of the nervous system has been well-established.[51–53] Among targets of H_2O_2 redox signaling are transcription factors of the Wnt and the Shh pathways.[54] Moreover, H_2O_2 has been recently discovered to be a signaling molecule controlling axonal path finding in zebrafish[54] and neuronal-growth-cone collapse *in vitro*.[55] Hence, it is not surprising that a *TMX2*-variant-mediated misbalance in oxidative eustress/distress could result in impaired neuronal development.

Under our experimental conditions, increased concentrations of H_2O_2 in the culture medium induced wild-type TMX2 dimerization. In the same maleimide alkylation assays, the TMX2 redox state does not seem sensitive to ER stressors. These results reflect a physiological sensitivity of TMX2 to H_2O_2, possibly mimicking an adaptive response to oxidative eustress, regulating physiological steps in development.[52,54] The wild-type TMX2 dimer was still slightly present under β-mercaptoethanol reducing conditions (Figure S6), indicating that it is partially formed through inter-disulfide bonds. The occurrence of homo-dimerization of other members of the PDI superfamily has been described earlier (for PDI,[56–58] PDIp,[59] and ERp29[60]) and is suggested as a general mechanism to regulate PDI function.[13,56] Dimers can exhibit higher chaperone or unfolding activity as described for ERp29, PDIp, CNX, and CRT dimerization.[60] Also, homodimerization of other TMX proteins has been postulated, e.g., a putative TMX1 homodimer was observed in immunoprecipitates with anti-CNX after ablation of the TRX domain active cysteines.[61]

Our data suggest the formation of TMX2 homo-dimer/polymers, on the basis of the evidence that observed TMX2 molecular masses on gradient gels show linearity with the predicted molecular mass by the Lambin method calculation and on the fact that the dimerization is not strictly dependent on disulfide bridge formation. Both under DTT pre-treatment in culture (of the TMX2 mutants) and by running a gel with β-mercaptoethanol, dimers are still present with an identical linear molecular mass. Because dimerization still occurs in the TRX domain mutant independently of an active cysteine and H_2O_2 treatment, the dimer does not represent a heterodimer of TMX2 with a substrate formed through mixed disulfides, similar to what is described for TMX1 homo-dimerization.[61] Although polymers were also observed after ablation of the TRX domain cysteine, they were barely present under reducing conditions. Hence, we cannot exclude interactions of TMX2 with other substrates of identical molecular mass, through TRX-domain-independent interactions. For example, N-linked glycosylation has been shown to modulate the formation of PDI polymers, and in TMX2 it could mediate interaction with heterologous peptides.[56]

Similar to in wild-type TMX2 under oxidative stress, we observed constitutive TMX2 homodi-/polymerization upon expression of the *TMX2* pathogenic variants (p.Arg53Cys and p.Arg231Trp), leading to mitochondrial dysfunction, reduced maximal respiration, and increased glycolysis, as seen under ER stress conditions.[7,50,62] However, we did not detect activation of UPR in fibroblasts from affected individuals, both under native and under treatment with H_2O_2 (data not shown). This suggests that the UPR is not the primary target of TMX2 function or that cultured fibroblasts are not the ideal test model.

Another fascinating aspect is TMX2 involvement in the pathogenesis of PMG. This malformation has long been considered as a defect of postmigratory cortical organization,[63] with wide genetic heterogeneity, but it is also a proven consequence of prenatal brain injury or disruptive events.[64] These aspects make genetic counseling of PMG most challenging. At brain imaging, it might be difficult to distinguish PMG resulting from environmental factors (e.g., prenatal CMV infection) or from genetic defects. At MRI and pathological examination, the main PMG characteristics are many small gyri with a pebbled appearance, loss of normal cortical lamination, overfolding and fusion of the gyri, and stippling of the white-gray matter border,[65] sometimes giving the appearance of generally thickened cortex. The cobblestone malformation is characterized by

a pebbled cerebral surface, thick cortex, and striations perpendicular to the cortical surface, which reflect tracks of neuroglial cells overmigrating above the glia limitans in the subarachnoid space; overmigration is sometimes massive and leads to thinning of the cortical plate.[35,66] The cobblestone malformation is frequently associated with cerebellar and pons dysplasia and variable hydrocephalus, as well as white matter and callosal dysgenesis. PMG and the cobblestone malformation have been sporadically reported to coexist in the same genetic disorder.[67,68] Pathology of the brain in two *TMX2*-variant affected individuals shows complete disorganization of the cortical layers (unlayered PMG) in both and, in one of them (P10), diffusely overmigrating neurons, typical of the cobblestone malformation, together with scattered white matter calcifications and pseudocysts, suggestive of a disruptive (CMV-like) event. Unlayered PMG is supposed to be caused by an early disruption of cortical development between 16–24 weeks gestation[69] and can also be observed in metabolic causes of PMG such as Zellweger disease (a peroxisomal biogenesis disorder characterized by mislocalization of catalase), or lining non-genetic schizencephalic clefts.[64,70] A mixture of disruptive and developmental migratory abnormalities has been reported for the brain disorder caused by the Zika virus (ZIKV) infection, where the effect on neuronal proliferation and migration is more prominent than in other more common congenital infections, i.e., CMV.[71] We demonstrate that TMX2-related PMG is a disorder of neuronal migration and cortical organization, without evidence of vascular or inflammatory disruption; in some cases it presents with a radiological aspect resembling an infectious, i.e., non-genetic, cause, and in other cases it microscopically shows the cobblestone malformation. These observations support the view that PMG and cobblestone are cortical malformations that can share a common pathogenesis and represent different severity of the spectrum.[72,73]

It is possible that some of the TMX2-related malformations are caused by a lack of physiological response to regulators of neuronal development (hypothetically H_2O_2-mediated axonal pathfinding), and some are the effect of abnormal oxidoreductase-mediated protein folding and calcium homeostasis, with a secondary mitochondrial dysfunction. Although no UPR stimulation was found in TMX2-deficient cells, TMX2 also plays a role in regulation of UPR and apoptosis, both mechanisms essential for regulation of neuronal proliferation and cortical organization.[74]

Our observation shows how, in humans, a genetic disorder of cellular redox adaptation mechanisms can be the cause of neuronal proliferation and migration disorders with characteristics of a disruptive event. These studies also provide a mechanistic explanation for the fact that human brain development is driven by steps strictly regulated in time and space, including individual response to environmental stimuli, e.g., to redox signaling molecules and changes in cellular redox state. PDI family members might prove to be major players in this process.

Accession Numbers

WES data are deposited internally at the Erasmus MC and in each medical institute that referred the affected individuals, out of respect for the privacy of the families. The mass spectrometry proteomics data have been deposited in the ProteomeXchange Consortium[75] via the PRIDE[76] partner repository with the dataset identifier PRIDE: PXD014064. The accession number for the RNA-seq data reported in this paper is GEO: GSE133483.

Supplemental Data

Supplemental Data can be found online at https://doi.org/10.1016/j.ajhg.2019.10.009.

Acknowledgements

We thank the families for participating in this study. This publication is, in part, a result of collaboration within the European Network on Brain Malformations funded by COST (European Cooperation in Science and Technology, Action CA16118). We thank Dr. Mark Nellist for sharing materials for IP experiments, Drs. Jeroen A.A. Demmers and Dick H.W. Dekkers of the Proteomics Center core facility, Erasmus University Medical Center, for help with mass spectrometry, Dr. Frans W. Verheijen for critically reading the manuscript, and Professor Dr Robert Hofstra for continuous support. We thank the Erasmus MC Cancer Computational Biology Center for giving access to their IT infrastructure and the software that was used for various computations and data analyses in this study.

L.V.V. was supported by Steunfonds Marguerite-Marie Delacroix, Research Foundation Flanders (FWO travel grant V429317N) and COST Action CA16118 (STSM grant #39032). S.B. is supported by the COST Action CA16118 (STSM grant #576). E.B.Y. is supported by the COST Action CA16118 (STSM grant #39362). A.F., D.T.P., N.B.B., R.O., M.H.L., H.K., A.C.J., N.J.M., and G.M.S.M. are members of the European Network on Brain Malformations, Neuro-MIG (COST Action CA16118). A.E.F. and D.T.P. were supported by the Newlife Foundation for Disabled Children (Grant reference: 11-12/04), Wales Epilepsy Research Network, and Wales Gene Park. A.C.J. is supported by a Senior Clinical Investigator Fellowship from the FWO. G.M.S.M. is supported by the ZonMW TOP grant #91217045 and by private donations. Data from families 8, 9, and 10 were collected as part of the SYNaPS Study Group collaboration funded by The Wellcome Trust and strategic award (Synaptopathies) funding (WT093205 MA and WT104033AIA). This research was conducted as part of the Queen Square Genomics group at University College London, supported by the National Institute for Health Research University College London Hospitals Biomedical Research Centre. The studies were funded by the Medical Research Council (MRC) (MR/S01165X/1, MR/S005021/1, and G0601943), the National Institute for Health Research University College London Hospitals Biomedical Research Centre, the Rosetree Trust, Ataxia UK, the Multiple System Atrophy (MSA) Trust, Brain Research UK, Sparks Great Ormand Street Hospital (GOSH) Charity, Muscular Dystrophy UK (MDUK), and the Muscular Dystrophy Association (MDA USA).

Declaration of Interests

The authors declare no competing interests.

Received: June 4, 2019
Accepted: October 11, 2019
Published: November 14, 2019

Web Resources

Allen Brain Atlas, http://human.brain-map.org/
Burrows-Wheeler Aligner (BWA), http://bio-bwa.sourceforge.net/
The Database for Annotation, Visualization and Integrated Discovery (DAVID), https://david.ncifcrf.gov/
dbSNP, https://www.ncbi.nlm.nih.gov/SNP/
ExAc Database, http://exac.broadinstitute.org
Gene Expression Omnibus, https://www.ncbi.nlm.nih.gov/geo/
GeneMatcher, https://www.genematcher.org
Genome Analysis Toolkit, https://www.broadinstitute.org/gatk/
gnomAD Database, http://gnomad.broadinstitute.org
Ingenuity, https://www.qiagen.com/us/shop/analytics-software/biological-data-tools/ingenuity-pathway-analysis/#orderinginformation
Mouse Genome Informatics, http://www.informatics.jax.org/
National Heart, Lung, and Blood Institute (NHLBI) Exome Sequencing Project (ESP), https://evs.gs.washington.edu/EVS/
Online Mendelian Inheritance in Man, https://www.omim.org/
PRoteomics IDEntifications (PRIDE) Database, https://www.ebi.ac.uk/pride/archive/
R, https://www.R-project.org/

References

1. Gutiérrez, T., and Simmen, T. (2018). Endoplasmic reticulum chaperones tweak the mitochondrial calcium rheostat to control metabolism and cell death. Cell Calcium *70*, 64–75.
2. Pisoni, G.B., Ruddock, L.W., Bulleid, N., and Molinari, M. (2015). Division of labor among oxidoreductases: TMX1 preferentially acts on transmembrane polypeptides. Mol. Biol. Cell *26*, 3390–3400.
3. Galligan, J.J., and Petersen, D.R. (2012). The human protein disulfide isomerase gene family. Hum. Genomics *6*, 6.
4. Ellgaard, L., and Ruddock, L.W. (2005). The human protein disulphide isomerase family: Substrate interactions and functional properties. EMBO Rep. *6*, 28–32.
5. Okumura, M., Kadokura, H., and Inaba, K. (2015). Structures and functions of protein disulfide isomerase family members involved in proteostasis in the endoplasmic reticulum. Free Radic. Biol. Med. *83*, 314–322.
6. Sugiura, Y., Araki, K., Iemura, S., Natsume, T., Hoseki, J., and Nagata, K. (2010). Novel thioredoxin-related transmembrane protein TMX4 has reductase activity. J. Biol. Chem. *285*, 7135–7142.
7. Raturi, A., Gutiérrez, T., Ortiz-Sandoval, C., Ruangkittisakul, A., Herrera-Cruz, M.S., Rockley, J.P., Gesson, K., Ourdev, D., Lou, P.H., Lucchinetti, E., et al. (2016). TMX1 determines cancer cell metabolism as a thiol-based modulator of ER-mitochondria Ca2+ flux. J. Cell Biol. *214*, 433–444.
8. Halperin, L., Jung, J., and Michalak, M. (2014). The many functions of the endoplasmic reticulum chaperones and folding enzymes. IUBMB Life *66*, 318–326.
9. Carreras-Sureda, A., Pihán, P., and Hetz, C. (2018). Calcium signaling at the endoplasmic reticulum: Fine-tuning stress responses. Cell Calcium *70*, 24–31.
10. Lynes, E.M., Bui, M., Yap, M.C., Benson, M.D., Schneider, B., Ellgaard, L., Berthiaume, L.G., and Simmen, T. (2012). Palmitoylated TMX and calnexin target to the mitochondria-associated membrane. EMBO J. *31*, 457–470.
11. Vance, J.E. (2014). MAM (mitochondria-associated membranes) in mammalian cells: Lipids and beyond. Biochim. Biophys. Acta *1841*, 595–609.
12. Andreu, C.I., Woehlbier, U., Torres, M., and Hetz, C. (2012). Protein disulfide isomerases in neurodegeneration: From disease mechanisms to biomedical applications. FEBS Lett. *586*, 2826–2834.
13. Parakh, S., and Atkin, J.D. (2015). Novel roles for protein disulphide isomerase in disease states: A double edged sword? Front. Cell Dev. Biol. *3*, 30.
14. Perri, E.R., Thomas, C.J., Parakh, S., Spencer, D.M., and Atkin, J.D. (2016). The unfolded protein response and the role of protein disulfide isomerase in neurodegeneration. Front. Cell Dev. Biol. *3*, 80.
15. Rauch, F., Fahiminiya, S., Majewski, J., Carrot-Zhang, J., Boudko, S., Glorieux, F., Mort, J.S., Bächinger, H.P., and Moffatt, P. (2015). Cole-Carpenter syndrome is caused by a heterozygous missense mutation in P4HB. Am. J. Hum. Genet. *96*, 425–431.
16. Abdel-Salam, G., Thoenes, M., Afifi, H.H., Körber, F., Swan, D., and Bolz, H.J. (2014). The supposed tumor suppressor gene WWOX is mutated in an early lethal microcephaly syndrome with epilepsy, growth retardation and retinal degeneration. Orphanet J. Rare Dis. *9*, 12.
17. Zolotushko, J., Flusser, H., Markus, B., Shelef, I., Langer, Y., Heverin, M., Björkhem, I., Sivan, S., and Birk, O.S. (2011). The desmosterolosis phenotype: Spasticity, microcephaly and micrognathia with agenesis of corpus callosum and loss of white matter. Eur. J. Hum. Genet. *19*, 942–946.
18. Hoefs, S.J., Skjeldal, O.H., Rodenburg, R.J., Nedregaard, B., van Kaauwen, E.P., Spiekerkötter, U., von Kleist-Retzow, J.C., Smeitink, J.A., Nijtmans, L.G., and van den Heuvel, L.P. (2010). Novel mutations in the NDUFS1 gene cause low residual activities in human complex I deficiencies. Mol. Genet. Metab. *100*, 251–256.
19. Wortmann, S.B., Vaz, F.M., Gardeitchik, T., Vissers, L.E.L.M., Renkema, G.H., Schuurs-Hoeijmakers, J.H.M., Kulik, W., Lammens, M., Christin, C., Kluijtmans, L.A.J., et al. (2012). Mutations in the phospholipid remodeling gene SERAC1 impair mitochondrial function and intracellular cholesterol trafficking and cause dystonia and deafness. Nat. Genet. *44*, 797–802.
20. Larrea, D., Pera, M., Gonnelli, A., Quintana-Cabrera, R., Akman, H.O., Guardia-Laguarta, C., Velasco, K.R., Area-Gomez, E., Dal Bello, F., De Stefani, D., et al. (2019). MFN2 mutations in Charcot-Marie-Tooth disease alter mitochondria-associated ER membrane function but do not impair bioenergetics. Hum. Mol. Genet. *28*, 1782–1800.
21. Meng, X., Zhang, C., Chen, J., Peng, S., Cao, Y., Ying, K., Xie, Y., and Mao, Y. (2003). Cloning and identification of a novel cDNA coding thioredoxin-related transmembrane protein 2. Biochem. Genet. *41*, 99–106.
22. Chao, R., Nevin, L., Agarwal, P., Riemer, J., Bai, X., Delaney, A., Akana, M., JimenezLopez, N., Bardakjian, T., Schneider, A., et al. (2010). A male with unilateral microphthalmia reveals a role for TMX3 in eye development. PLoS ONE *5*, e10565.
23. Sobreira, N., Schiettecatte, F., Valle, D., and Hamosh, A. (2015). GeneMatcher: A matching tool for connecting investigators with an interest in the same gene. Hum. Mutat. *36*, 928–930.

24. Zillhardt, J.L., Poirier, K., Broix, L., Lebrun, N., Elmorjani, A., Martinovic, J., Saillour, Y., Muraca, G., Nectoux, J., Bessieres, B., et al. (2016). Mosaic parental germline mutations causing recurrent forms of malformations of cortical development. Eur. J. Hum. Genet. *24*, 611–614.
25. Judaš, M., Šimić, G., Petanjek, Z., Jovanov-Milošević, N., Pletikos, M., Vasung, L., Vukšić, M., and Kostović, I. (2011). The Zagreb Collection of human brains: A unique, versatile, but underexploited resource for the neuroscience community. Ann. N Y Acad. Sci. *1225* (*Suppl 1*), E105–E130.
26. Dobin, A., Davis, C.A., Schlesinger, F., Drenkow, J., Zaleski, C., Jha, S., Batut, P., Chaisson, M., and Gingeras, T.R. (2013). STAR: Ultrafast universal RNA-seq aligner. Bioinformatics *29*, 15–21.
27. Liao, Y., Smyth, G.K., and Shi, W. (2014). featureCounts: An efficient general purpose program for assigning sequence reads to genomic features. Bioinformatics *30*, 923–930.
28. Robinson, M.D., McCarthy, D.J., and Smyth, G.K. (2010). edgeR: A Bioconductor package for differential expression analysis of digital gene expression data. Bioinformatics *26*, 139–140.
29. Huang, W., Sherman, B.T., and Lempicki, R.A. (2009). Systematic and integrative analysis of large gene lists using DAVID bioinformatics resources. Nat. Protoc. *4*, 44–57.
30. Huang, W., Sherman, B.T., and Lempicki, R.A. (2009). Bioinformatics enrichment tools: Paths toward the comprehensive functional analysis of large gene lists. Nucleic Acids Res. *37*, 1–13.
31. Oegema, R., Baillat, D., Schot, R., van Unen, L.M., Brooks, A., Kia, S.K., Hoogeboom, A.J.M., Xia, Z., Li, W., Cesaroni, M., et al. (2017). Human mutations in integrator complex subunits link transcriptome integrity to brain development. PLoS Genet. *13*, e1006809.
32. Vandervore, L.V., Schot, R., Kasteleijn, E., Oegema, R., Stouffs, K., Gheldof, A., Grochowska, M.M., van der Sterre, M.L.T., van Unen, L.M.A., Wilke, M., et al. (2019). Heterogeneous clinical phenotypes and cerebral malformations reflected by rotatin cellular dynamics. Brain *142*, 867–884.
33. Milanese, C., Payán-Gómez, C., Galvani, M., Molano González, N., Tresini, M., Nait Abdellah, S., van Roon-Mom, W.M.C., Figini, S., Marinus, J., van Hilten, J.J., and Mastroberardino, P.G. (2019). Peripheral mitochondrial function correlates with clinical severity in idiopathic Parkinson's disease. Mov. Disord. *34*, 1192–1202.
34. Matsuo, Y., and Hirota, K. (2017). Transmembrane thioredoxin-related protein TMX1 is reversibly oxidized in response to protein accumulation in the endoplasmic reticulum. FEBS Open Bio *7*, 1768–1777.
35. Devisme, L., Bouchet, C., Gonzalès, M., Alanio, E., Bazin, A., Bessières, B., Bigi, N., Blanchet, P., Bonneau, D., Bonnières, M., et al. (2012). Cobblestone lissencephaly: Neuropathological subtypes and correlations with genes of dystroglycanopathies. Brain *135*, 469–482.
36. Zhang, Z., Xin, D., Wang, P., Zhou, L., Hu, L., Kong, X., and Hurst, L.D. (2009). Noisy splicing, more than expression regulation, explains why some exons are subject to nonsense-mediated mRNA decay. BMC Biol. *7*, 23.
37. Zou, W., Bai, Y., Wang, X., Cheng, K., Sun, H., Zhang, G., Wang, X., and Yang, Z. (2017). PERK-phosphorylated eIF2α pathway suppresses tumor metastasis through downregulating expression of Programmed Death Ligand 1 and CXCL5 in triple-negative breast cancer. Cancer Biother. Radiopharm. *32*, 282–287.
38. Gade, P., Ramachandran, G., Maachani, U.B., Rizzo, M.A., Okada, T., Prywes, R., Cross, A.S., Mori, K., and Kalvakolanu, D.V. (2012). An IFN-γ-stimulated ATF6-C/EBP-β-signaling pathway critical for the expression of Death Associated Protein Kinase 1 and induction of autophagy. Proc. Natl. Acad. Sci. USA *109*, 10316–10321.
39. Nita, I., Hostettler, K., Tamo, L., Medová, M., Bombaci, G., Zhong, J., Allam, R., Zimmer, Y., Roth, M., Geiser, T., and Gazdhar, A. (2017). Hepatocyte growth factor secreted by bone marrow stem cell reduce ER stress and improves repair in alveolar epithelial II cells. Sci. Rep. *7*, 41901.
40. Wolters, P.J., Collard, H.R., and Jones, K.D. (2014). Pathogenesis of idiopathic pulmonary fibrosis. Annu. Rev. Pathol. *9*, 157–179.
41. Wu, R., Zhang, Q.-H., Lu, Y.-J., Ren, K., and Yi, G.-H. (2015). Involvement of the IRE1α-XBP1 pathway and XBP1s-dependent transcriptional reprogramming in metabolic diseases. DNA Cell Biol. *34*, 6–18.
42. Jessop, C.E., Watkins, R.H., Simmons, J.J., Tasab, M., and Bulleid, N.J. (2009). Protein disulphide isomerase family members show distinct substrate specificity: P5 is targeted to BiP client proteins. J. Cell Sci. *122*, 4287–4295.
43. Horna-Terrón, E., Pradilla-Dieste, A., Sánchez-de-Diego, C., and Osada, J. (2014). TXNDC5, a newly discovered disulfide isomerase with a key role in cell physiology and pathology. Int. J. Mol. Sci. *15*, 23501–23518.
44. Lakkaraju, A.K., Abrami, L., Lemmin, T., Blaskovic, S., Kunz, B., Kihara, A., Dal Peraro, M., and van der Goot, F.G. (2012). Palmitoylated calnexin is a key component of the ribosome-translocon complex. EMBO J. *31*, 1823–1835.
45. Harbauer, A.B., Zahedi, R.P., Sickmann, A., Pfanner, N., and Meisinger, C. (2014). The protein import machinery of mitochondria-a regulatory hub in metabolism, stress, and disease. Cell Metab. *19*, 357–372.
46. Liu, J., Wang, Y., Song, L., Zeng, L., Yi, W., Liu, T., Chen, H., Wang, M., Ju, Z., and Cong, Y.-S. (2017). A critical role of DDRGK1 in endoplasmic reticulum homoeostasis via regulation of IRE1α stability. Nat. Commun. *8*, 14186.
47. Lambin, P. (1978). Reliability of molecular weight determination of proteins by polyacrylamide gradient gel electrophoresis in the presence of sodium dodecyl sulfate. Anal. Biochem. *85*, 114–125.
48. Gilady, S.Y., Bui, M., Lynes, E.M., Benson, M.D., Watts, R., Vance, J.E., and Simmen, T. (2010). Ero1alpha requires oxidizing and normoxic conditions to localize to the mitochondria-associated membrane (MAM). Cell Stress Chaperones *15*, 619–629.
49. Yoshihara, E., Chen, Z., Matsuo, Y., Masutani, H., and Yodoi, J. (2010). Thiol redox transitions by thioredoxin and thioredoxin-binding protein-2 in cell signaling. Methods Enzymol. *474*, 67–82.
50. Sies, H. (2017). Hydrogen peroxide as a central redox signaling molecule in physiological oxidative stress: Oxidative eustress. Redox Biol. *11*, 613–619.
51. Winterbourn, C.C. (2018). Biological production, detection, and fate of hydrogen peroxide. Antioxid. Redox Signal. *29*, 541–551.
52. Olguín-Albuerne, M., and Morán, J. (2018). Redox signaling mechanisms in nervous system development. Antioxid. Redox Signal. *28*, 1603–1625.
53. Oswald, M.C.W., Garnham, N., Sweeney, S.T., and Landgraf, M. (2018). Regulation of neuronal development and function by ROS. FEBS Lett. *592*, 679–691.

54. Gauron, C., Meda, F., Dupont, E., Albadri, S., Quenech'Du, N., Ipendey, E., Volovitch, M., Del Bene, F., Joliot, A., Rampon, C., and Vriz, S. (2016). Hydrogen peroxide (H2O2) controls axon pathfinding during zebrafish development. Dev. Biol. *414*, 133–141.
55. Morinaka, A., Yamada, M., Itofusa, R., Funato, Y., Yoshimura, Y., Nakamura, F., Yoshimura, T., Kaibuchi, K., Goshima, Y., Hoshino, M., et al. (2011). Thioredoxin mediates oxidation-dependent phosphorylation of CRMP2 and growth cone collapse. Sci. Signal. *4*, ra26.
56. Walker, A.K., Soo, K.Y., Levina, V., Talbo, G.H., and Atkin, J.D. (2013). N-linked glycosylation modulates dimerization of protein disulfide isomerase family A member 2 (PDIA2). FEBS J. *280*, 233–243.
57. Solovyov, A., and Gilbert, H.F. (2004). Zinc-dependent dimerization of the folding catalyst, protein disulfide isomerase. Protein Sci. *13*, 1902–1907.
58. Bastos-Aristizabal, S., Kozlov, G., and Gehring, K. (2014). Structural insight into the dimerization of human protein disulfide isomerase. Protein Sci. *23*, 618–626.
59. Fu, X.M., and Zhu, B.T. (2009). Human pancreas-specific protein disulfide isomerase homolog (PDIp) is an intracellular estrogen-binding protein that modulates estrogen levels and actions in target cells. J. Steroid Biochem. Mol. Biol. *115*, 20–29.
60. Rainey-Barger, E.K., Mkrtchian, S., and Tsai, B. (2007). Dimerization of ERp29, a PDI-like protein, is essential for its diverse functions. Mol. Biol. Cell *18*, 1253–1260.
61. Matsuo, Y., Masutani, H., Son, A., Kizaka-Kondoh, S., and Yodoi, J. (2009). Physical and functional interaction of transmembrane thioredoxin-related protein with major histocompatibility complex class I heavy chain: redox-based protein quality control and its potential relevance to immune responses. Mol. Biol. Cell *20*, 4552–4562.
62. Hetz, C. (2012). The unfolded protein response: Controlling cell fate decisions under ER stress and beyond. Nat. Rev. Mol. Cell Biol. *13*, 89–102.
63. Barkovich, A.J., Guerrini, R., Kuzniecky, R.I., Jackson, G.D., and Dobyns, W.B. (2012). A developmental and genetic classification for malformations of cortical development: Update 2012. Brain *135*, 1348–1369.
64. Stutterd, C.A., and Leventer, R.J. (2014). Polymicrogyria: A common and heterogeneous malformation of cortical development. Am. J. Med. Genet. C. Semin. Med. Genet. *166C*, 227–239.
65. Leventer, R.J., Jansen, A., Pilz, D.T., Stoodley, N., Marini, C., Dubeau, F., Malone, J., Mitchell, L.A., Mandelstam, S., Scheffer, I.E., et al. (2010). Clinical and imaging heterogeneity of polymicrogyria: A study of 328 patients. Brain *133*, 1415–1427.
66. Brun, B.N., Mockler, S.R.H., Laubscher, K.M., Stephan, C.M., Wallace, A.M., Collison, J.A., Zimmerman, M.B., Dobyns, W.B., and Mathews, K.D. (2017). Comparison of brain MRI findings with language and motor function in the dystroglycanopathies. Neurology *88*, 623–629.
67. Bahi-Buisson, N., Poirier, K., Boddaert, N., Fallet-Bianco, C., Specchio, N., Bertini, E., Caglayan, O., Lascelles, K., Elie, C., Rambaud, J., et al. (2010). GPR56-related bilateral frontoparietal polymicrogyria: Further evidence for an overlap with the cobblestone complex. Brain *133*, 3194–3209.
68. Jaglin, X.H., Poirier, K., Saillour, Y., Buhler, E., Tian, G., Bahi-Buisson, N., Fallet-Bianco, C., Phan-Dinh-Tuy, F., Kong, X.P., Bomont, P., et al. (2009). Mutations in the beta-tubulin gene TUBB2B result in asymmetrical polymicrogyria. Nat. Genet. *41*, 746–752.
69. Barth, P.G. (1987). Disorders of neuronal migration. Canadian Journal of Neurological Sciences *14*, 1–16.
70. Liu, H.M., Bangaru, B.S., Kidd, J., and Boggs, J. (1976). Neuropathological considerations in cerebro-hepato-renal syndrome (Zellweger's syndrome). Acta Neuropathol. *34*, 115–123.
71. Melo, A.S.O., Aguiar, R.S., Amorim, M.M.R., Arruda, M.B., Melo, F.O., Ribeiro, S.T.C., Batista, A.G.M., Ferreira, T., Dos Santos, M.P., Sampaio, V.V., et al. (2016). Congenital zika virus infection: Beyond neonatal microcephaly. JAMA Neurol. *73*, 1407–1416.
72. Jansen, A.C., Robitaille, Y., Honavar, M., Mullatti, N., Leventer, R.J., Andermann, E., Andermann, F., and Squier, W. (2016). The histopathology of polymicrogyria: A series of 71 brain autopsy studies. Dev. Med. Child Neurol. *58*, 39–48.
73. Squier, W., and Jansen, A. (2014). Polymicrogyria: Pathology, fetal origins and mechanisms. Acta Neuropathol. Commun. *2*, 80.
74. Laguesse, S., Creppe, C., Nedialkova, D.D., Prévot, P.P., Borgs, L., Huysseune, S., Franco, B., Duysens, G., Krusy, N., Lee, G., et al. (2015). A dynamic unfolded protein response contributes to the control of cortical neurogenesis. Dev. Cell *35*, 553–567.
75. Deutsch, E.W., Csordas, A., Sun, Z., Jarnuczak, A., Perez-Riverol, Y., Ternent, T., Campbell, D.S., Bernal-Llinares, M., Okuda, S., Kawano, S., et al. (2017). The ProteomeXchange consortium in 2017: Supporting the cultural change in proteomics public data deposition. Nucleic Acids Res. *45* (D1), D1100–D1106.
76. Perez-Riverol, Y., Csordas, A., Bai, J., Bernal-Llinares, M., Hewapathirana, S., Kundu, D.J., Inuganti, A., Griss, J., Mayer, G., Eisenacher, M., et al. (2019). The PRIDE database and related tools and resources in 2019: improving support for quantification data. Nucleic Acids Res. *47* (D1), D442–D450.